

## Article

# Solid-State-Activated Sintering of $\text{ZnAl}_2\text{O}_4$ Ceramics Containing $\text{Cu}_3\text{Nb}_2\text{O}_8$ with Superior Dielectric and Thermal Properties

Koichi Shigeno <sup>1,\*</sup>, Takuma Yano <sup>1</sup> and Hirotaka Fujimori <sup>2</sup>

<sup>1</sup> National Institute of Technology (KOSEN), Ube College, 2-14-1 Tokiwadai, Ube, Yamaguchi 755-8555, Japan; ntnm.894@gmail.com

<sup>2</sup> Graduate School of Sciences and Technology for Innovation, Yamaguchi University, 2-16-1 Tokiwadai, Ube, Yamaguchi 755-8611, Japan; hiro@hiro-fuji.net

\* Correspondence: shigeno@ube-k.ac.jp; Tel./Fax: +81-836-35-5294

**Abstract:** Low-temperature co-fired ceramics (LTCCs) are dielectric materials that can be co-fired with Ag or Cu; however, conventional LTCC materials are mostly poorly thermally conductive, which is problematic and requires improvement. We focused on  $\text{ZnAl}_2\text{O}_4$  (gahnite) as a base material. With its high thermal conductivity ( $\sim 59 \text{ W}\cdot\text{m}^{-1}\cdot\text{K}^{-1}$  reported for  $0.83\text{ZnAl}_2\text{O}_4\text{-}0.17\text{TiO}_2$ ),  $\text{ZnAl}_2\text{O}_4$  is potentially more thermally conductive than  $\text{Al}_2\text{O}_3$  (alumina); however, it sinters densely at a moderate temperature ( $\sim 1500^\circ\text{C}$ ). The addition of only 4 wt.% of  $\text{Cu}_3\text{Nb}_2\text{O}_8$  significantly lowered the sintering temperature of  $\text{ZnAl}_2\text{O}_4$  to  $910^\circ\text{C}$ , which is lower than the melting point of silver ( $961^\circ\text{C}$ ). The sample fired at  $960^\circ\text{C}$  for 384 h exhibited a relative permittivity ( $\epsilon_r$ ) of 9.2, a quality factor by resonant frequency ( $Q \times f$ ) value of 105,000 GHz, and a temperature coefficient of the resonant frequency ( $\tau_f$ ) of  $-56 \text{ ppm}\cdot\text{K}^{-1}$ . The sample exhibited a thermal conductivity of  $10.1 \text{ W}\cdot\text{m}^{-1}\cdot\text{K}^{-1}$ , which exceeds that of conventional LTCCs ( $\sim 2\text{-}7 \text{ W}\cdot\text{m}^{-1}\cdot\text{K}^{-1}$ ); hence, it is a superior LTCC candidate. In addition, a mixed powder of the  $\text{Cu}_3\text{Nb}_2\text{O}_8$  additive and  $\text{ZnAl}_2\text{O}_4$  has a melting temperature that is not significantly different from that ( $\sim 970^\circ\text{C}$ ) of the pristine  $\text{Cu}_3\text{Nb}_2\text{O}_8$  additive. The sample appears to densify in the solid state through a solid-state-activated sintering mechanism.

**Keywords:**  $\text{ZnAl}_2\text{O}_4$  (gahnite); low-temperature co-fired ceramics (LTCCs); solid-state-activated sintering; microwave dielectric properties; thermal conductivity



**Citation:** Shigeno, K.; Yano, T.; Fujimori, H. Solid-State-Activated Sintering of  $\text{ZnAl}_2\text{O}_4$  Ceramics Containing  $\text{Cu}_3\text{Nb}_2\text{O}_8$  with Superior Dielectric and Thermal Properties. *Materials* **2022**, *15*, 1770. <https://doi.org/10.3390/ma15051770>

Academic Editor: Oleksandr Tkach

Received: 3 January 2022

Accepted: 23 February 2022

Published: 26 February 2022

**Publisher's Note:** MDPI stays neutral with regard to jurisdictional claims in published maps and institutional affiliations.



**Copyright:** © 2022 by the authors. Licensee MDPI, Basel, Switzerland. This article is an open access article distributed under the terms and conditions of the Creative Commons Attribution (CC BY) license (<https://creativecommons.org/licenses/by/4.0/>).

## 1. Introduction

Low-temperature co-fired ceramics (LTCCs) are dielectric materials that can be co-fired with Ag or Cu, which are metals that exhibit low-resistance conduction at temperatures below their melting points ( $961$  and  $1084^\circ\text{C}$ , respectively) [1,2]. LTCCs have been widely used in small electronic devices, such as wiring substrates and integrated circuit packages for high-frequency communication. With the aim of improving energy efficiency, ultralow-temperature co-fired ceramics (ULTCCs) that can be co-fired with Al at  $660^\circ\text{C}$  (below the melting point of Al) are currently being actively researched [3]. However, the poor heat-dissipation properties of LTCC materials are problematic because the temperature of semiconductors mounted on the LTCC materials rises, causing thermal runaway of these semiconductors. Aluminum-based oxide ceramics, such as  $\text{Al}_2\text{O}_3$  (alumina), are relatively highly thermally conductive; however, a large amount (approximately 50% or more of the total) of a poorly thermally conductive low-softening-point glass needs to be added to achieve low-temperature sintering when used as the base material. Consequently, the majority of these conventional LTCC materials are poorly thermally conductive (approximately  $2\text{-}7 \text{ W}\cdot\text{m}^{-1}\cdot\text{K}^{-1}$ ), which is a shortcoming [4,5]. The heat-generation densities of semiconductor-based electronic components, such as light-emitting diodes (LEDs), mounted on LTCC multilayer devices have recently been reported to be increasing [6,7];

hence, highly thermally conductive LTCC materials are in demand. We previously developed sintering additives for alumina using highly thermally conductive ( $\sim 30 \text{ W}\cdot\text{m}^{-1}\cdot\text{K}^{-1}$ ) alumina as a base material that, when added in small amounts, enables alumina to be sintered at low temperatures. As a result, we developed a  $\text{CuO-TiO}_2\text{-Nb}_2\text{O}_5\text{-Ag}_2\text{O}$  additive that facilitates alumina sintering at  $900 \text{ }^\circ\text{C}$  or less when added at 5 wt.%, thereby realizing highly thermally conductive ( $\sim 18\text{--}20 \text{ W}\cdot\text{m}^{-1}\cdot\text{K}^{-1}$ ) low-temperature co-fired alumina (LTCA) [8,9].

Furthermore, we also focused on  $\text{ZnAl}_2\text{O}_4$  (gahnite) as a base material; this aluminum-based oxide has good dielectric properties and is potentially more thermally conductive than alumina [10–16]. According to Surendran et al., a sample produced by firing a  $0.83\text{ZnAl}_2\text{O}_4\text{-}0.17\text{TiO}_2$  (molar ratio) composition at  $1440 \text{ }^\circ\text{C}$  exhibited a thermal conductivity of  $59 \text{ W}\cdot\text{m}^{-1}\cdot\text{K}^{-1}$  [11]. Consequently,  $\text{ZnAl}_2\text{O}_4$  is expected to be used as a novel highly thermally conductive LTCC substrate if it can be sintered at low temperature. Low-temperature sintering involving the addition of glass to  $\text{ZnAl}_2\text{O}_4$  [14] has been studied. The use of crystalline additives other than glass has also been studied a few times [16]; however, densely sintered  $\text{ZnAl}_2\text{O}_4$  has not been achieved below  $1100 \text{ }^\circ\text{C}$  yet. Therefore, we aimed to develop a sintering additive that, when added in small amounts, enables  $\text{ZnAl}_2\text{O}_4$  to be densely sintered below  $1000 \text{ }^\circ\text{C}$  (a low temperature).

We previously found that the addition of only 5 wt.%  $\text{CuO-Nb}_2\text{O}_5$  (in a 7:3 Cu:Nb molar ratio) led to a significantly lower sintering temperature ( $960 \text{ }^\circ\text{C}$ ) [17]. The sample fired at  $960 \text{ }^\circ\text{C}$  for 2 h exhibited a relative permittivity ( $\epsilon_r$ ) of 9.1, a quality factor by resonant frequency ( $Q \times f$ ) value of 30,000 GHz (at a frequency of  $\sim 13 \text{ GHz}$ ), a temperature coefficient of the resonant frequency ( $\tau_f$ ) of  $-69 \text{ ppm}\cdot\text{K}^{-1}$ , and a thermal conductivity ( $\kappa$ ) of  $9.3 \text{ W}\cdot\text{m}^{-1}\cdot\text{K}^{-1}$ , which are relatively satisfactory; however, these values can be further improved. Because the mixture of  $\text{CuO}$  and  $\text{Nb}_2\text{O}_5$  is separated at the atomic level, we postulate that small amounts of unreacted components exacerbate the  $Q \times f$  value of low-temperature sintered  $\text{ZnAl}_2\text{O}_4$ . In addition, the low-temperature sintering mechanism remains unknown. The composite oxide formed between a  $\text{ZnO}$  varistor and an  $\text{Al}_2\text{O}_3$  substrate by low-temperature sintering has also been recently examined [7];  $\text{ZnO}$  containing  $\text{Bi}_2\text{O}_3$  is known to react with  $\text{Al}_2\text{O}_3$  to produce  $\text{ZnAl}_2\text{O}_4$  [18]. Therefore, understanding the sintering behavior of  $\text{ZnAl}_2\text{O}_4$  from a practical perspective is also important.

This study has two objectives. The first involves further improving the dielectric properties and thermal conductivities of low-temperature sintered  $\text{ZnAl}_2\text{O}_4$  ceramics. To achieve this goal, we examined adding small quantities of calcined  $\text{Cu}_3\text{Nb}_2\text{O}_8$  [19], which has been reported to exhibit relatively good dielectric properties, instead of a mixture of  $\text{CuO}$  and  $\text{Nb}_2\text{O}_5$  in the same molar ratio, prolonging the holding time at each firing temperature. The second involves gaining insight into the low-temperature sintering mechanism. Specifically, we examined whether densification is promoted only in the solid phase or in other phases, including the liquid phase. In addition, we examined the densification role of each additive component (Cu and Nb).

## 2. Materials and Methods

### 2.1. Fabricating Sintered Samples

Figure 1a shows the flow process used to prepare gahnite sintered bodies containing additives. First, commercially available  $\text{Al}_2\text{O}_3$  and  $\text{ZnO}$  powders (99.99%, average particle size:  $1 \text{ }\mu\text{m}$  for each powder; Kojundo Chemical Laboratory Co., Ltd., Saitama, Japan) were mixed in a 1:1 molar ratio and ball-milled for 16 h, with water as the dispersion medium. The dried powder was then calcined at  $1100 \text{ }^\circ\text{C}$  for 4 h in air to yield  $\text{ZnAl}_2\text{O}_4$ , which was then pulverized using a ball mill for 48 h, with water as the dispersion medium. The dried powder was used as the raw material, as shown in Figure 1b; its specific surface area was determined to be  $8.65 \text{ m}^2/\text{g}$  by the Brunauer–Emmett–Teller (BET) method (AUTOSORB-1, Spectris Co., Ltd., Kanagawa, Japan). According to the BET measurements and assuming particles were spherical [20], the average particle size was approximately  $0.2 \text{ }\mu\text{m}$ .

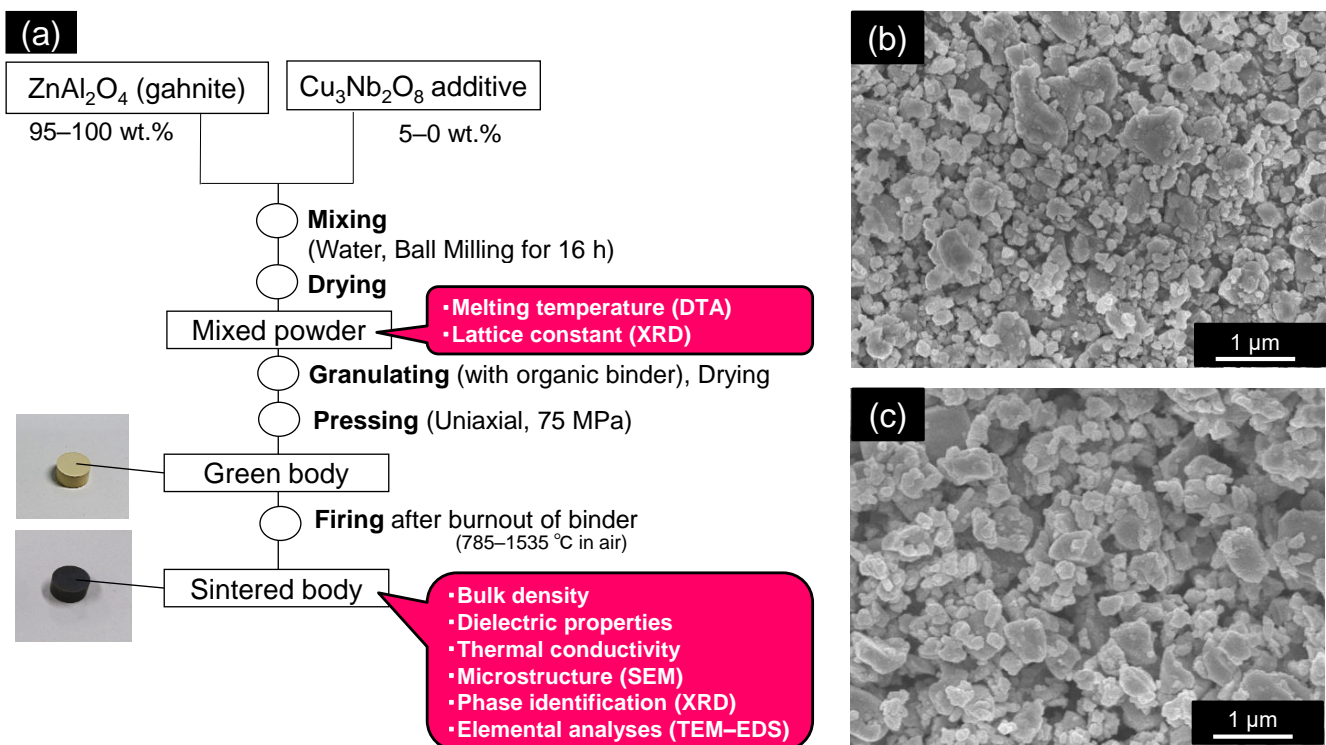


**Figure 1.** (a) Experimental process for preparing ZnAl<sub>2</sub>O<sub>4</sub> ceramics containing the Cu<sub>3</sub>Nb<sub>2</sub>O<sub>8</sub> sintering aid. (b) Scanning electron microscopy (SEM) image of the ZnAl<sub>2</sub>O<sub>4</sub> raw material powder. (c) SEM image of the Cu<sub>3</sub>Nb<sub>2</sub>O<sub>8</sub> raw material powder.

Table 1 lists the 14 main samples characterized in this study, as well as their synthesis conditions, and the purpose of each characteristic comparison. Commercially available CuO (99.3%, Nissin Chemco Ltd., Kyoto, Japan) and Nb<sub>2</sub>O<sub>5</sub> (99.9%, Kojundo Chemical Laboratory Co., Ltd., Saitama, Japan) powders were mixed in a 3:2 Cu:Nb molar ratio and ball-milled for 16 h, with water as the dispersion medium. The dried powder was calcined at 835 °C for 2 h in air to yield Cu<sub>3</sub>Nb<sub>2</sub>O<sub>8</sub>, which was pulverized using a ball mill for 48 h, with water as the dispersion medium. The dried powder was used as the additive, as shown in Figure 1c. ZnAl<sub>2</sub>O<sub>4</sub> powder (100–95 wt.%) and the Cu<sub>3</sub>Nb<sub>2</sub>O<sub>8</sub> additive powder (0–5 wt.%) were mixed and ball-milled for 16 h, with water as the dispersion medium. We set the maximum additive concentration to 5 wt.% because we found that this quantity provided sufficiently well-sintered samples in our previous study [17]. For reference, ball-milling was conducted with yttria-stabilized zirconia (YSZ) balls in a polyethylene bottle at a rotation rate of 160 rpm.

The dried powder was granulated with polyvinyl alcohol (PVA, DKS Co., Ltd., Kyoto, Japan) binder and formed into a disc through uniaxial pressing at 75 MPa. The weight ratio of the dried powder–PVA binder was set to be 100:4. The green bodies were fired at 785–1535 °C in air for the required time (between 10 min and 384 h). The effects of sintering-aided calcination on sinterability and the dielectric and thermal properties were investigated. Specifically, ZnAl<sub>2</sub>O<sub>4</sub> samples were fabricated by separately adding CuO and Nb<sub>2</sub>O<sub>5</sub> (5 wt.% in total) in the same Cu:Nb molar ratio (3:2) as Cu<sub>3</sub>Nb<sub>2</sub>O<sub>8</sub> (referred to as “non-calcined” in Table 1). For reference, we also prepared a sintered body calcined at 885 °C for 2 h using only the Cu<sub>3</sub>Nb<sub>2</sub>O<sub>8</sub> additive powder. For reference, the heating and cooling rates used for calcination and firing were both set to 300 °C/h.

**Table 1.** ZnAl<sub>2</sub>O<sub>4</sub> and additive quantities, additive conditions, firing temperatures, holding times, and comparison purposes of the main 14 samples examined in this study. Comparison purposes: \*1) clarifying the effect of additive quantities for well-sintered samples; \*2) clarifying the effect of firing temperature for samples of the same composition (ZnAl<sub>2</sub>O<sub>4</sub> with 5 wt.% of calcined additive); \*3) clarifying the effect of additive calcination; \*4) clarifying the effect of prolonging holding times for samples fired at 910, 935, and 960 °C (retention times: 2 and 384 h).

Sample	ZnAl <sub>2</sub> O <sub>4</sub> Quantity	Additive Quantity	Additive Conditions	Firing Temperature	Holding Time	Comparison Purpose
		wt. %		°C	h	
G01	100	0	Calcined	1485	2	*1)
G02	99	1	Calcined	1185	2	*1)
G03	98	2	Calcined	1085	2	*1)
G04	97	3	Calcined	1035	2	*1)
G05	96	4	Calcined	960	2	*1) *4)
G06	95	5	Calcined	785	2	*2)
G07	95	5	Calcined	960	2	*1) *2) *3)
G08	95	5	Non-calcined	960	2	*3)
G09	96	4	Calcined	910	2	*4)
G10	96	4	Calcined	910	384	*4)
G11	96	4	Calcined	935	2	*4)
G12	96	4	Calcined	935	384	*4)
G13	96	4	Calcined	960	384	*4)
G14	0	100	Calcined	885	2	*1)

## 2.2. Characterization

The properties of the prepared sintered bodies were evaluated on the basis of their ceramic densities, microwave dielectric properties, and thermal conductivities. The ceramic densities were measured using the geometrical method. The theoretical density ( $\rho$ ) of each sample was calculated using the following equation:

$$\rho = \frac{W_1 + W_2}{\left(\frac{W_1}{\rho_1}\right) + \left(\frac{W_2}{\rho_2}\right)}, \quad (1)$$

where  $W_1$  and  $W_2$ , are the weight percentages of ZnAl<sub>2</sub>O<sub>4</sub> and Cu<sub>3</sub>Nb<sub>2</sub>O<sub>8</sub>, respectively, and  $\rho_1$  and  $\rho_2$  are the densities of ZnAl<sub>2</sub>O<sub>4</sub> (4.606 g/cm<sup>3</sup>) and Cu<sub>3</sub>Nb<sub>2</sub>O<sub>8</sub> (5.655 g/cm<sup>3</sup>), respectively [21]. Relative density was calculated by dividing the measured ceramic density by the theoretical density. Three major parameters that describe microwave dielectric properties, namely, the relative permittivity ( $\epsilon_r$ ), the quality factor by resonant frequency ( $Q \times f$ ), and the temperature coefficient of the resonant frequency ( $\tau_f$ ), were measured using the Hakki–Coleman method [22] with a network analyzer (8720ES, Agilent Technologies, Santa Clara, CA, USA).  $\tau_f$  values were calculated using the following equation:

$$\tau_f = \frac{1}{f(T_0)} \cdot \frac{f(T_1) - f(T_0)}{T_1 - T_0}, \quad (2)$$

where  $f(T_0)$  and  $f(T_1)$  are the resonant frequencies at 20 and 80 °C, respectively. Thermal conductivities were measured using the xenon flash method (LFA447, Netzsch, Selb, Germany). To discuss sinterability, as well as the microwave dielectric properties and thermal conductivities of the developed materials, we observed their microstructures by scanning electron microscopy (SEM; JSM-7600F, JEOL Ltd., Tokyo, Japan) at an accelerating

voltage of 5 kV. To prepare samples for SEM, the samples were polished with 0.5  $\mu\text{m}$  diamond abrasives, followed by thermal etching for 1 h at a temperature 50  $^{\circ}\text{C}$  lower than each firing temperature. The average grain size ( $D_g$ ) was measured by the planimetric method [20,23] for at least 200 grains. In addition, we identified their crystalline phases via X-ray diffractometry (XRD; Ultima IV, Rigaku Co., Ltd., Tokyo, Japan) augmented with a Cu-K $\alpha$  radiation source at 40 kV and 40 mA in the  $2\theta$  range of 20–60 $^{\circ}$  with a step size of 0.02 $^{\circ}$  and a rate of 4 $^{\circ}\cdot\text{min}^{-1}$ .

To further discuss the sintering mechanism, the melting temperatures of the mixed powders were determined by differential thermal analysis (DTA; Thermo Plus Evo II, Shimadzu Co., Ltd., Kyoto, Japan). The lattice constants of  $\text{ZnAl}_2\text{O}_4$  and  $\text{Cu}_3\text{Nb}_2\text{O}_8$  in the mixed powders were determined via a step scanning method of XRD augmented with a Cu-K $\alpha$  radiation source at 40 kV and 30 mA in the  $2\theta$  range of 10–110 $^{\circ}$  with a step size of 0.02 $^{\circ}$  and a counting time of 7 s/step, with  $\text{LaB}_6$  (SRM660b, NIST) as the internal standard. In addition, the fired samples were placed on Mo mesh and thinned by focused ion beam (FIB) milling (JEM-9320FIB, JEOL Ltd., Tokyo, Japan) with Ga ions to yield  $\sim 100$  nm thick flakes; these flakes are half the average particle diameter of the raw  $\text{ZnAl}_2\text{O}_4$  powder in size. For the samples thinned by FIB milling, transmission electron microscopy (TEM) at an accelerating voltage of 200 keV and energy-dispersive spectroscopy (EDS; JEM-2100, JEOL Ltd., Tokyo, Japan) were used to analyze the microstructures of the sintered samples and their elemental distributions.

### 3. Results and Discussion

#### 3.1. Effect of the $\text{Cu}_3\text{Nb}_2\text{O}_8$ Additive and Its Calcination on the Properties of $\text{ZnAl}_2\text{O}_4$

We first evaluated the effect of the added  $\text{Cu}_3\text{Nb}_2\text{O}_8$  and the properties of the  $\text{ZnAl}_2\text{O}_4$  sample. Figure 2 shows the relationship between the firing temperature and ceramic densities of  $\text{ZnAl}_2\text{O}_4$  alone, and  $\text{ZnAl}_2\text{O}_4$  containing 1, 2, 3, 4, and 5 wt.% of the  $\text{Cu}_3\text{Nb}_2\text{O}_8$  additive; samples were held for 2 h at each temperature. A firing temperature of 1485  $^{\circ}\text{C}$  was required for  $\text{ZnAl}_2\text{O}_4$  to produce a dense sintered body in the absence of the sintering aid. On the other hand, significantly lower sintering temperatures were required for  $\text{ZnAl}_2\text{O}_4$  containing the  $\text{Cu}_3\text{Nb}_2\text{O}_8$  additive; that is, dense sintered bodies with relative densities of 95% or more were obtained for samples containing 4 wt.% or more of the sintering aid when fired at 960  $^{\circ}\text{C}$  for 2 h. This temperature is only 1  $^{\circ}\text{C}$  lower than the melting point of metallic silver (961  $^{\circ}\text{C}$ ); therefore, these bodies do not fully meet LTCC material requirements. However, they can be improved by prolonging the holding time at a lower firing temperature (see Section 3.2).

Table 2 lists the additive quantities, additive conditions, firing temperatures, densities, average grain sizes ( $D_g$ ), dielectric properties ( $\epsilon_r$ ,  $Q \times f$ ,  $\tau_f$ ), and thermal conductivities ( $\kappa$ ) of the main 14 samples (G01–14) examined in this study. For reference, typical data of a conventional LTCC ( $\text{Al}_2\text{O}_3$  + glass) substrate are shown as sample R01. In addition, Figure 3 shows SEM images of polished surfaces that depict the microstructures of the sintered bodies. Figure 3a shows that the  $\text{ZnAl}_2\text{O}_4$  sample fired at 1485  $^{\circ}\text{C}$  for 2 h (G01) contained grains approximately 1–2  $\mu\text{m}$  in size ( $D_g$ : 2.10  $\mu\text{m}$ ), which are larger than the grains of the raw powder (Figure 1b). However, submicron-sized voids were observed at various locations. Figure 3b,c show  $\text{ZnAl}_2\text{O}_4$  sintered bodies containing 5 wt.% of the  $\text{Cu}_3\text{Nb}_2\text{O}_8$  additive. The sample fired at 785  $^{\circ}\text{C}$  for 2 h (G06) exhibited almost no necking between particles, with many voids present (Figure 3b). On the other hand, the sample fired at 960  $^{\circ}\text{C}$  for 2 h (G07) contained angular particles and few voids. The grains in Figure 3c ( $D_g$ : 0.55  $\mu\text{m}$ ) are larger than those in Figure 3b ( $D_g$ : 0.20  $\mu\text{m}$ ); however, they are still submicron in size. We conclude that the sample fired at 960  $^{\circ}\text{C}$  was densified. In addition, TEM–EDS (Figure 4) revealed that the Cu and Nb of the additive segregated at the grain boundaries; however, Cu was detected inside the  $\text{ZnAl}_2\text{O}_4$  grains in some places.

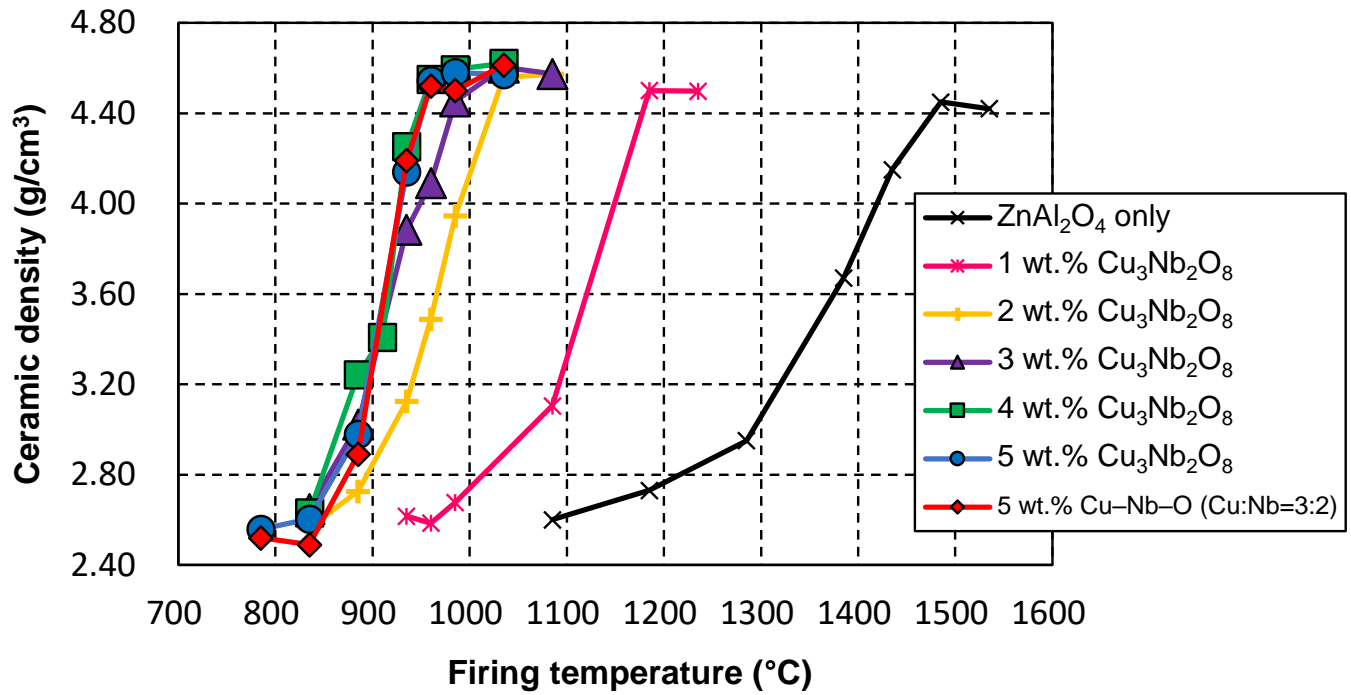


**Figure 2.** Ceramic densities of pristine  $ZnAl_2O_4$ ,  $ZnAl_2O_4$  containing 1, 2, 3, 4, and 5 wt.% of the  $Cu_3Nb_2O_8$  additive, and  $ZnAl_2O_4$  containing 5 wt.% of the  $CuO-Nb_2O_5$  (Cu:Nb = 3:2 (molar ratio)) additive as functions of firing temperature. The holding time at each temperature: 2 h.

**Table 2.** Additive quantities and conditions, firing temperatures, densities, average grain sizes ( $D_g$ ), dielectric properties ( $\epsilon_r, Q \times f, \tau_f$ ), and thermal conductivities ( $\kappa$ ) of the samples examined in this study; “×” indicates that the values of  $\epsilon_r$  and  $Q \times f$  of the sample (G06) were unable to be determined due to their significantly low values; “××” indicates that the values of  $\tau_f$  and  $\kappa$  for the samples (G06, G09, and G11) with insufficient ceramic densities (relative densities less than 95%) were not measured. R01\* is an example of a conventional LTCC substrate.

Sample	Additive Quantity	Additive Conditions	Firing Temp.	Holding Time	Ceramic Density	Relative Density	$D_g$	$\epsilon_r$	$Q \times f$	$\tau_f$	$\kappa$
	wt.%		°C	h	g/cm <sup>3</sup>	%	μm	—	GHz	ppm·K <sup>-1</sup>	W·m <sup>-1</sup> ·K <sup>-1</sup>
G01	0	Calcined	1485	2	4.47	97.0	2.10	9.0	16,100	−73	27.3
G02	1	Calcined	1185	2	4.50	97.5	3.10	9.0	98,200	−63	12.2
G03	2	Calcined	1085	2	4.57	98.9	1.36	9.1	81,700	−60	10.2
G04	3	Calcined	1035	2	4.60	99.4	0.89	9.3	77,000	−60	8.8
G05	4	Calcined	960	2	4.55	98.1	0.53	9.1	65,300	−54	8.9
G06	5	Calcined	785	2	2.56	55.0	0.20	×	×	××	××
G07	5	Calcined	960	2	4.55	97.8	0.55	9.2	60,800	−56	7.9
G08	5	Non-calcined	960	2	4.52	97.2	0.57	9.0	51,300	−63	8.5
G09	4	Calcined	910	2	3.41	73.5	0.30	6.0	2480	××	××
G10	4	Calcined	910	384	4.57	98.6	1.15	9.0	71,500	−54	11.3
G11	4	Calcined	935	2	4.01	86.4	0.41	8.0	7840	××	××
G12	4	Calcined	935	384	4.62	99.5	1.79	9.3	93,300	−61	10.2
G13	4	Calcined	960	384	4.57	98.5	2.60	9.2	105,000	−56	10.1
G14	100	Calcined	885	2	5.37	95.0	10.1	15.1	18,700	−70	6.1
R01*	—	—	900–1100 [4]	—	—	—	—	<15 [4,5]	>1000 [4]	<±100 [4]	2–7 [4,5]

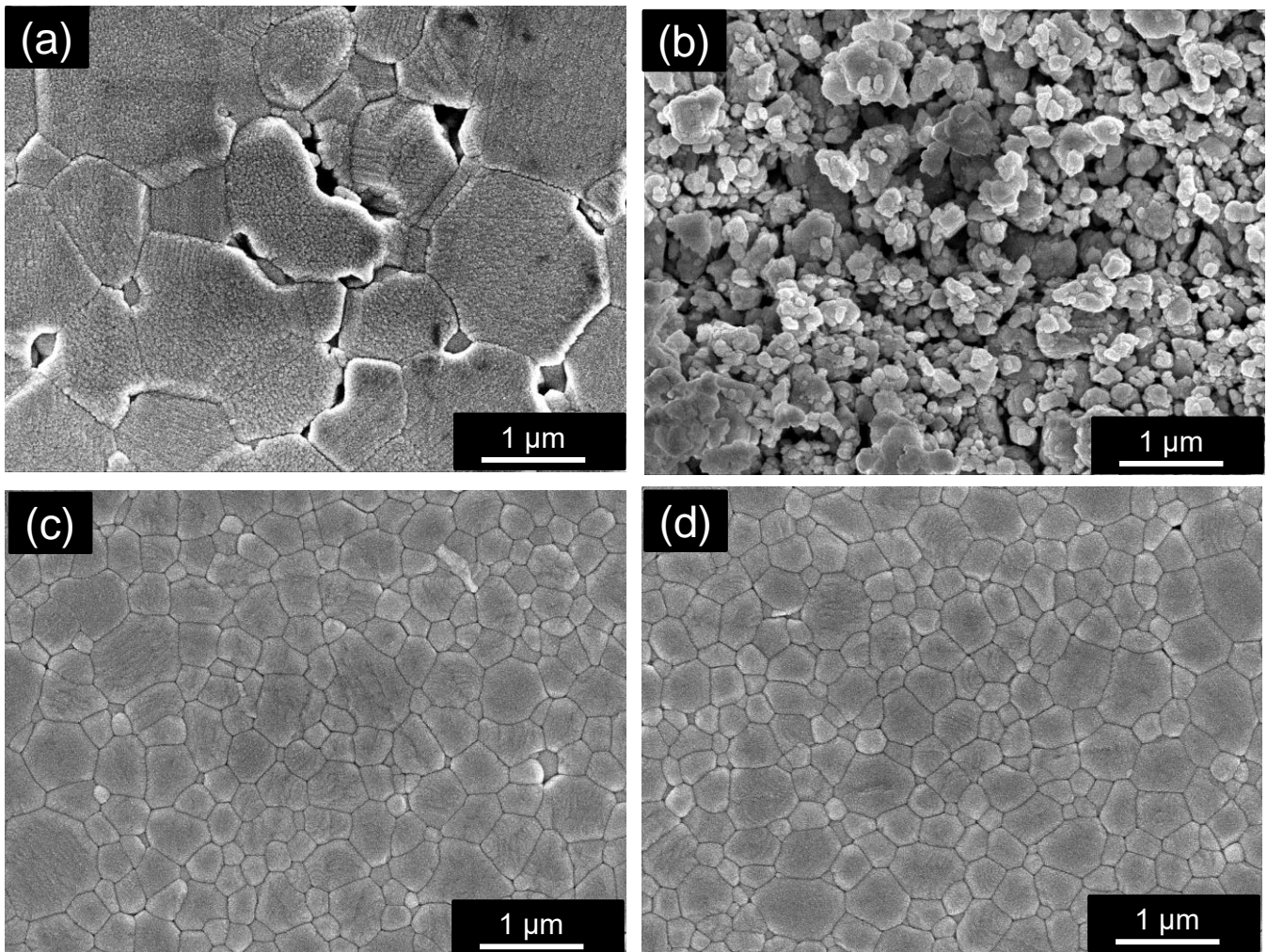


**Figure 3.** SEM images of polished surfaces of (a) pristine  $\text{ZnAl}_2\text{O}_4$  fired at  $1485^\circ\text{C}$  for 2 h (sample G01), (b)  $\text{ZnAl}_2\text{O}_4$  containing 5 wt.% of the  $\text{Cu}_3\text{Nb}_2\text{O}_8$  additive fired at  $785^\circ\text{C}$  for 2 h (G06), (c)  $\text{ZnAl}_2\text{O}_4$  containing 5 wt.% of the  $\text{Cu}_3\text{Nb}_2\text{O}_8$  additive fired at  $960^\circ\text{C}$  for 2 h (G07), and (d)  $\text{ZnAl}_2\text{O}_4$  containing 5 wt.% of the  $\text{CuO-Nb}_2\text{O}_5$  (Cu:Nb = 3:2 (molar ratio)) additive fired at  $960^\circ\text{C}$  for 2 h (G08).

As summarized in Table 2, samples G01–G05 and G07 were all well sintered, with relative densities in excess of 95%. Little change was observed in  $\epsilon_r$  with increasing amount of sintering aid. On the other hand, the  $Q \times f$  of the  $\text{ZnAl}_2\text{O}_4$  sample with 1 wt.% additive (G02, 98,200 GHz) was approximately sixfold higher than that of the additive-free sample (G01, 16,100 GHz), and decreased with further increases in additive quantity (G03–05 and G07). However, the  $Q \times f$  value of sample G07 was observed to be 50,000 GHz or higher, even with 5 wt.% of the additive, which is a good value for low-temperature sintered ceramics. As has been extensively discussed, the main origins of the dielectric loss tangent ( $\tan \delta$ : reciprocal of the  $Q$  value) of an actual dielectric ceramic at microwave frequency is mainly determined by an intrinsic factor (the anharmonic terms of the crystal's potential energy) and extrinsic factors (lattice defects caused by impurities, disordered charge distribution in the crystal, grain boundaries, random grain orientation, microcracks, porosity, etc.) [24–26]. Considering the above viewpoint, the relative density of sample G01 was 97.0%; hence, it was 3.0% porous. In addition, Figure 3a shows grains and void diameters that are sufficiently large to be recognizable in the SEM image. In other words, we believe that this sample contained many extrinsic dielectric loss factors associated with its porosity. The addition of 1 wt.% of the sintering aid decreased the number of voids in the sintered  $\text{ZnAl}_2\text{O}_4$  (observed in Figure 3a), which reduced lattice relaxation and increased

its  $Q \times f$  value. Penn et al. reported that dielectric loss depends strongly on pore volume, with only a small degree of porosity markedly affecting the loss of sintered alumina [26]. They also mentioned that loss may be related to the surface area of the pores, as the alumina at the surface of a pore is in a different environment to the alumina within the matrix. The presence of a free surface (such as a pore) leads to crystal lattice relaxation. The relaxed surface is effectively different from that of the bulk material and is, therefore, likely to have a different  $\tan \delta$  (one of the extrinsic factors of dielectric loss). This study also supports our views on  $\text{ZnAl}_2\text{O}_4$  (above), an Al-based oxide. Further increases in additive quantity probably resulted in higher degrees of lattice defects in the  $\text{ZnAl}_2\text{O}_4$  due to Cu-component incorporation (see Section 3.3.2); hence, lower  $Q \times f$  values were observed. In addition, the  $Q \times f$  values of the samples were also affected by the relatively low  $Q \times f$  of the  $\text{Cu}_3\text{Nb}_2\text{O}_8$  additive itself (G14, 18,700 GHz), which was presumably lower than that of  $\text{ZnAl}_2\text{O}_4$  (106,000 GHz, reported by Zheng et al. [25]).

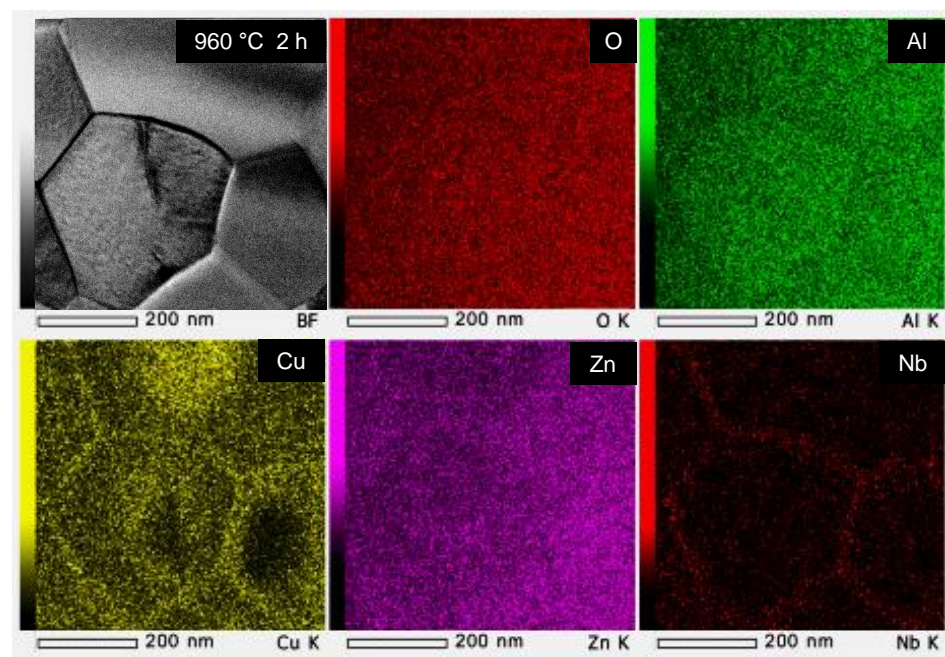


**Figure 4.** TEM image and EDS elemental maps of  $\text{ZnAl}_2\text{O}_4$  containing 5 wt.%  $\text{Cu}_3\text{Nb}_2\text{O}_8$  fired at 960 °C for 2 h (G07).

On the other hand,  $\tau_f$  was observed to increase slightly with increasing additive quantity compared with the value for the pristine  $\text{ZnAl}_2\text{O}_4$  sample; that is, the sample devoid of additive (G01) exhibited a  $\tau_f$  value of  $-73 \text{ ppm}\cdot\text{K}^{-1}$ , whereas sample G07, with 5 wt.% of the additive, exhibited a value of  $-56 \text{ ppm}\cdot\text{K}^{-1}$ . The  $\text{Cu}_3\text{Nb}_2\text{O}_8$  additive itself (G14) had a  $\tau_f$  of  $-70 \text{ ppm}\cdot\text{K}^{-1}$ , which is almost the same as that of the additive-free sample (G01); the additive quantity was also small. Therefore, we conclude that the cause of the observed trend rested with the base material rather than the additive and presume that the solid solution of the Cu component in  $\text{ZnAl}_2\text{O}_4$  was involved.  $\kappa$  was also observed to decrease monotonically with increasing additive quantity. In particular, the  $\kappa$  value of the sample containing 1 wt.% of additive (G02) was dramatically lower (by a factor of two) compared to that of the additive-free sample (G01). On the basis of our previous research, we believe that the solid solution of the Cu component in  $\text{ZnAl}_2\text{O}_4$  was responsible for this observation [17].

We next examined the  $\text{ZnAl}_2\text{O}_4$  sample containing 5 wt.% of the  $\text{CuO-Nb}_2\text{O}_5$  (Cu:Nb = 3:2 (molar ratio)) sintering aid, and compared various characteristics of its calcined and uncalcined samples. As shown in Figure 2, we did not detect any difference in the sintering behavior of the uncalcined (G08) and calcined (G07) samples. The SEM image in Figure 3d

reveals that the microstructure of the uncalcined sample (G08) was almost identical to that of calcined G07 shown in Figure 3c; both exhibited almost no voids and submicron-sized grains (for G08,  $D_g = 0.57 \mu\text{m}$ ). The dielectric and thermal data summarized in Table 2 reveal no significant differences in the relative permittivities,  $\tau_f$  values, and thermal conductivities of G07 and G08; however, calcined sample G07 showed a higher  $Q \times f$  value (60,800 GHz) than that of uncalcined sample G08 (51,300 GHz). Furthermore, Figure 5 shows that the two exhibited almost no difference in relative permittivity, whereas the calcined sample exhibited higher  $Q \times f$  values at firing temperatures of 935, 960, 985, and 1035 °C.

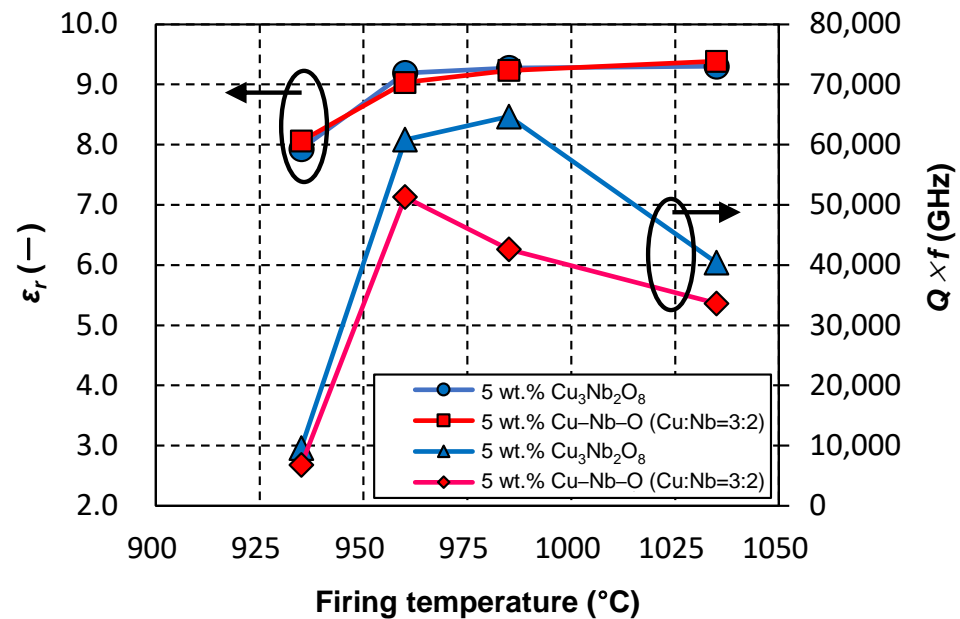


**Figure 5.** Effect of Cu–Nb–O additive (Cu:Nb = 3:2 (molar ratio)) calcination on the relationship linking firing temperature, relative permittivity, and the  $Q \times f$  of  $\text{ZnAl}_2\text{O}_4$  containing 5 wt.% of the additive. A 2 h holding time was applied at each temperature.

The  $Q \times f$  value of  $\text{ZnAl}_2\text{O}_4$  appeared to depend on whether or not the  $\text{CuO-Nb}_2\text{O}_5$  additive was calcined; hence, the reason for this dependence was investigated by XRD. Figure 6a shows XRD patterns of the G01, G06, G07, G13, G08, and G14 sintered bodies, with Figure 6b showing enlarged patterns. The unknown peaks indicated by solid circles (●) near  $2\theta = 30^\circ$  and around  $2\theta = 33^\circ$  were also observed in the pattern of the pure  $\text{ZnAl}_2\text{O}_4$  sample (G01). Therefore, we conclude that these peaks are not directly related to the observed characteristic change. Peaks corresponding to  $\text{Cu}_3\text{Nb}_2\text{O}_8$  were observed for the calcined sample (G06) fired at 785 °C for 2 h, as well as for the sample (G07) fired at 960 °C for 2 h, although they were less intense in the case of the latter. In addition, unknown peaks, indicated by solid triangles (▲), were clearly observed. The XRD peaks observed for G06 and G07 were slightly shifted compared to those of the pure  $\text{Cu}_3\text{Nb}_2\text{O}_8$  sintered body (G14). For example, the 121 reflection, which can be observed at  $2\theta = 32.6^\circ$  in the XRD pattern of  $\text{Cu}_3\text{Nb}_2\text{O}_8$ , was observed at lower angles in the patterns of G06 and G07. According to Kim et al. [19], such a shift is consistent with a solid solution in which Zn occupies Cu sites in  $\text{Cu}_3\text{Nb}_2\text{O}_8$ . However, the same report revealed no significant change in the  $Q \times f$  value due to the formation of the Zn solid solution. No peaks corresponding to  $\text{Cu}_3\text{Nb}_2\text{O}_8$  were observed for the sample with the uncalcined additive (G08) fired at 960 °C for 2 h. In addition, peaks corresponding to  $\text{Zn}_3\text{Nb}_2\text{O}_8$  were not observed.  $\text{Cu}_3\text{Nb}_2\text{O}_8$  and  $\text{Zn}_3\text{Nb}_2\text{O}_8$  reportedly exhibit relatively high  $Q \times f$  values of approximately 50,000 and 80,000 GHz, respectively [19]. In other words, the formed  $\text{Cu}_3\text{Nb}_2\text{O}_8$  and  $\text{Zn}_3\text{Nb}_2\text{O}_8$  exhibit relatively high  $Q \times f$  values when the sintered body is fabricated by the separate addition of sintering aids, such as CuO and  $\text{Nb}_2\text{O}_5$ . We, therefore, conclude that compounds related to CuO,  $\text{Nb}_2\text{O}_5$ , or ZnO, with lower  $Q \times f$  values, were formed in the current work, which we

presume to be the cause of the observed  $Q \times f$  trend. Clearly, these results alone cannot identify the cause of the observed trend, and further detailed analysis is required.

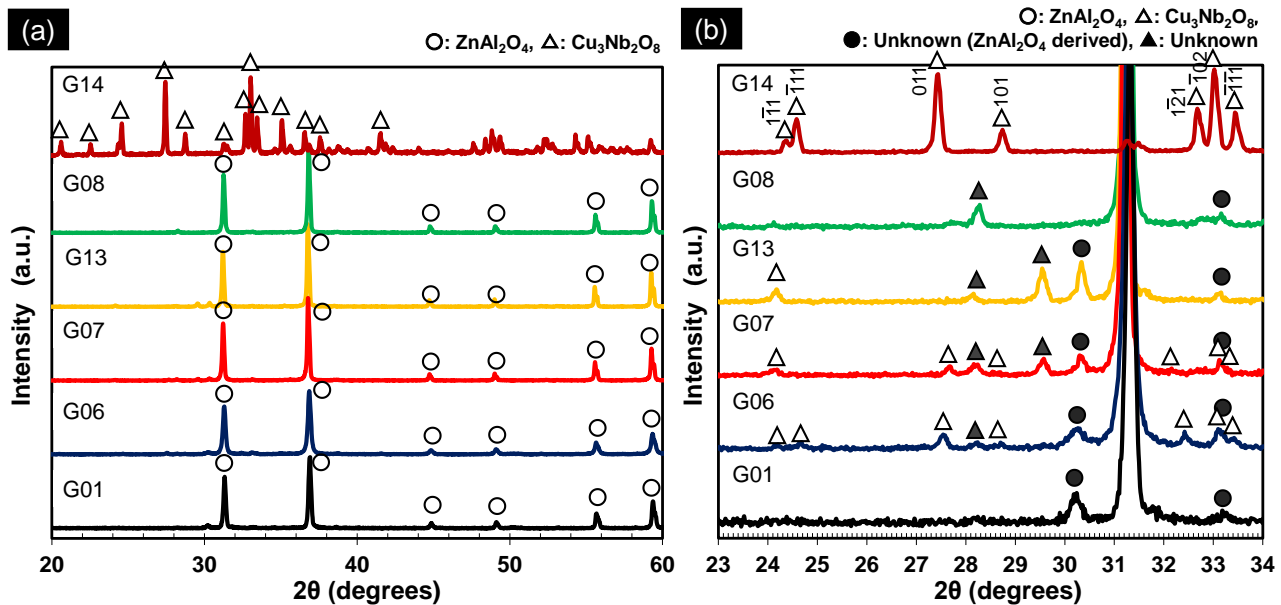


**Figure 6.** (a) XRD patterns of pristine  $\text{ZnAl}_2\text{O}_4$  fired at  $1485^\circ\text{C}$  for 2 h (G01),  $\text{ZnAl}_2\text{O}_4$  containing 5 wt.% of the  $\text{Cu}_3\text{Nb}_2\text{O}_8$  additive fired at  $785^\circ\text{C}$  for 2 h (G06),  $\text{ZnAl}_2\text{O}_4$  containing 5 wt.% of the  $\text{Cu}_3\text{Nb}_2\text{O}_8$  additive fired at  $960^\circ\text{C}$  for 2 h (G07),  $\text{ZnAl}_2\text{O}_4$  containing 4 wt.% of the  $\text{Cu}_3\text{Nb}_2\text{O}_8$  additive fired at  $960^\circ\text{C}$  for 384 h (G13),  $\text{ZnAl}_2\text{O}_4$  containing 5 wt.% of the  $\text{CuO-Nb}_2\text{O}_5$  ( $\text{Cu:Nb} = 3:2$  (molar ratio)) additive fired at  $960^\circ\text{C}$  for 2 h (G08), and pristine  $\text{Cu}_3\text{Nb}_2\text{O}_8$  fired at  $885^\circ\text{C}$  for 2 h (G14). (b) Enlarged XRD patterns of G01, G06, G07, G13, G08, and G14 in panel (a).  $\text{Cu}_3\text{Nb}_2\text{O}_8$  diffraction indices are indicated in the figure.

### 3.2. Effect of Holding Time on the Properties of $\text{ZnAl}_2\text{O}_4$

Figure 2 shows that  $\text{ZnAl}_2\text{O}_4$  sinterability saturated when more than 4 wt.%  $\text{Cu}_3\text{Nb}_2\text{O}_8$  was added. Therefore, the  $\text{Cu}_3\text{Nb}_2\text{O}_8$  quantity was fixed at 4 wt.% and the effects of retention time at 910, 935, and  $960^\circ\text{C}$ , which are below the melting point of Ag, were investigated. As discussed in detail in the next section (Section 3.3), these temperatures were also lower than the melting temperature of the additive. Figure 7a reveals that the ceramic densities of the samples in this system were significantly affected by the time held at the firing temperature; that is, dense sintered bodies were obtained by holding for an extended time (384 h) even at firing temperatures less than or equal to  $960^\circ\text{C}$  (e.g.,  $910^\circ\text{C}$ ). Figure 7b,c show relative permittivity and  $Q \times f$  data, while Table 2 summarizes sample properties (G05, G09–G13). Relative permittivity (Figure 7b) exhibited almost identical behavior to sintered body density (Figure 7a), with relative permittivity and density observed to saturate concurrently. On the other hand, the  $Q \times f$  value (Figure 7c) rose sharply to a value of 60,000 GHz or higher (e.g., for G05 and G10) when the ceramic density of the sample exceeded a threshold value of  $4.4\text{--}4.5\text{ g/cm}^3$ . In addition,  $Q \times f$  increased further with increasing holding time, even at the same density. The  $Q \times f$  of the sample fired at  $960^\circ\text{C}$  for 384 h (G13) was determined to be 105,000 GHz (at a frequency of  $\sim 13\text{ GHz}$ ). This trend was also observed for samples fired for 384 h at lower temperatures (910 and  $935^\circ\text{C}$ ) (G10: 71,500, G12: 93,300 GHz). Moreover, the thermal conductivity of G13 exceeded  $10\text{ W}\cdot\text{m}^{-1}\cdot\text{K}^{-1}$  ( $10.1\text{ W}\cdot\text{m}^{-1}\cdot\text{K}^{-1}$ ), which is approximately 10% higher than that of the sample fired at  $960^\circ\text{C}$  for 2 h (G05). This trend was also observed for the samples fired at lower temperatures (910, and  $935^\circ\text{C}$ ) for 384 h (G10: 11.3, G12:  $10.2\text{ W}\cdot\text{m}^{-1}\cdot\text{K}^{-1}$ ); hence, G10, G12, and G13 are excellent LTCC candidate materials.

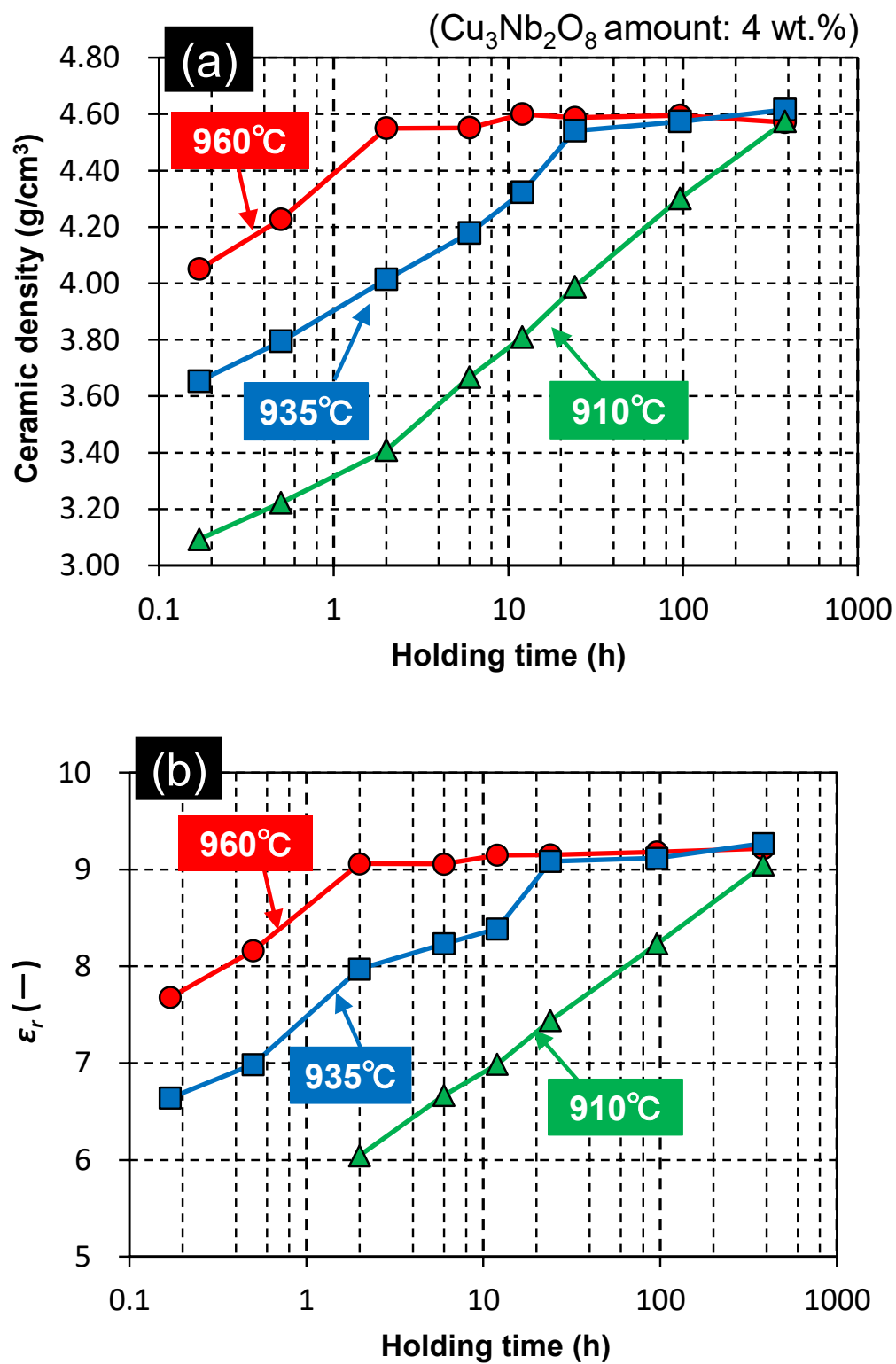
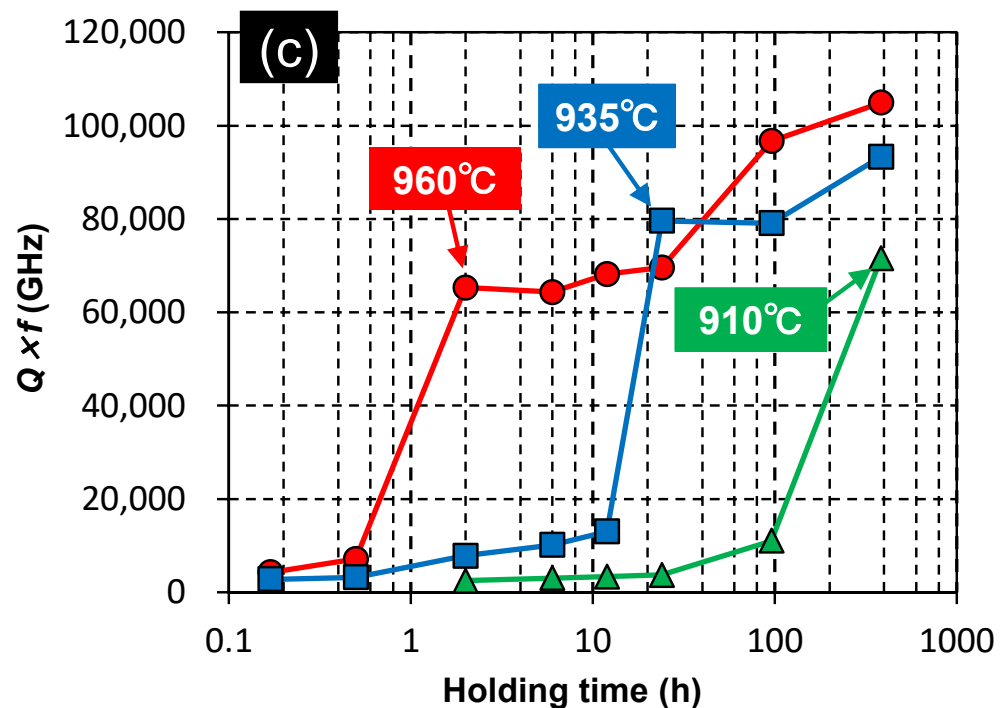
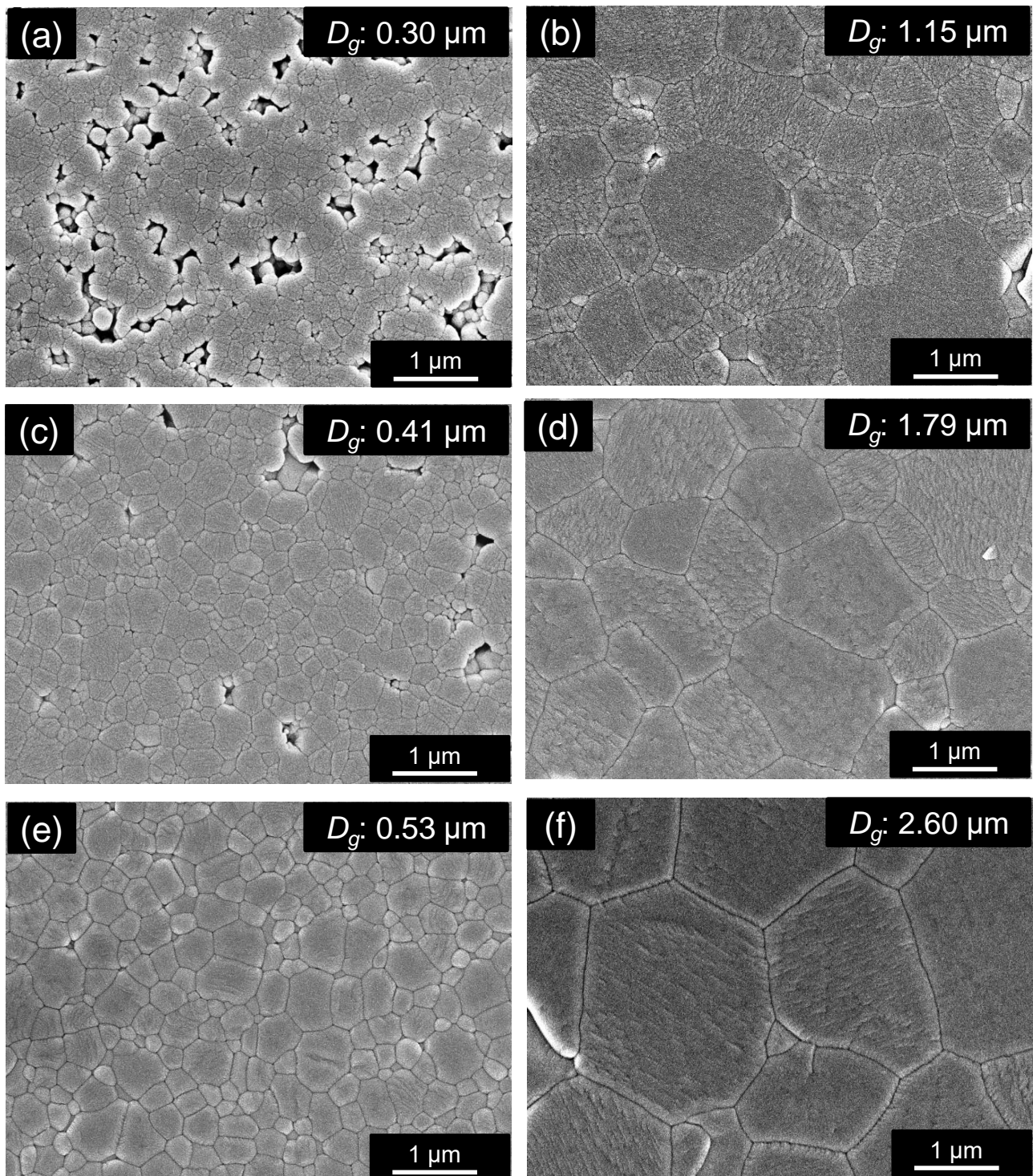


Figure 7. Cont.



**Figure 7.** Ceramic densities and microwave dielectric and thermal properties of  $\text{ZnAl}_2\text{O}_4$  containing 4 wt.% of  $\text{Cu}_3\text{Nb}_2\text{O}_8$  as a function of holding time at firing temperatures of 910, 935, and 960 °C: (a) ceramic density; (b) relative permittivity  $\epsilon_r$ ; (c)  $Q \times f$ .

The reason for the observed increases in  $Q \times f$  and thermal conductivity with prolonged holding time is discussed in terms of the SEM-observed sample microstructures. First, Figure 8a,c,e, reveal that all samples prepared with a retention time of 2 h (G09, G11, and G05) had submicron-sized grains, with higher firing temperatures leading to fewer voids. Almost no visible voids were observed in the sample fired at 960 °C for 2 h (G05). We presume that the porosity of the  $\text{ZnAl}_2\text{O}_4$  sintered body suppresses crystal lattice relaxation (one of extrinsic factors of dielectric loss) [26]; hence, porosity is responsible for the higher  $Q \times f$  of sample G05 compared with that of samples G09 and G11. Figure 8b,d,f reveal that the samples prepared with a retention time of 384 h (G10, G12, and G13) exhibited almost no voids. On the other hand, remarkable grain growth was observed, and many particles were larger than 1  $\mu\text{m}$ ; higher firing temperatures led to larger grains. Figure 8e,f compare the morphologies of the samples fired at 960 °C for 2 h (G05) and at 960 °C for 384 h (G13); hardly any voids and almost identical sintering densities were observed. On the other hand, sample G13 had the highest  $Q \times f$  value in this study; it exhibited much higher grain growth ( $D_g$ : 2.60  $\mu\text{m}$ ) than G05 ( $D_g$ : 0.53  $\mu\text{m}$ ), with many particles larger than 2  $\mu\text{m}$ . Therefore, larger grains may lead to fewer grain boundaries per unit volume (one of the extrinsic factors of dielectric loss) and higher  $Q \times f$  values, which seem to have reduced the extrinsic dielectric loss factors and led to an equivalent  $Q \times f$  value (106,000 GHz [25]) to that reported for pure  $\text{ZnAl}_2\text{O}_4$ . However, in the above study, the  $Q \times f$  value was calculated to be 394,000 GHz when only the intrinsic factor was considered; hence, eliminating the influence of extrinsic factors remains an important issue. In addition, phonons have longer mean free paths that result in high heat conduction; we consider this to be related to the higher  $Q \times f$  and thermal conductivity of the sample. For reference, the XRD pattern in Figure 6b shows that the phases generated in G13 (other than  $\text{ZnAl}_2\text{O}_4$ ) at a retention time of 384 h were the same type as those observed for G08 (with a composition almost identical to that G05 with a retention time of 2 h), although their peak intensities were different. Identifying clear causes on the basis of these generated phases is a future objective.



**Figure 8.** SEM images of polished surfaces of ZnAl<sub>2</sub>O<sub>4</sub> containing 4 wt.% of the Cu<sub>3</sub>Nb<sub>2</sub>O<sub>8</sub> additive fired at (a) 910 °C for 2 h (G09), (b) 910 °C for 384 h (G10), (c) 935 °C for 2 h (G11), (d) 935 °C for 384 h (G12), (e) 960 °C for 2 h (G05), and (f) 960 °C for 384 h (G13). The average grain size ( $D_g$ ) of each sample is also shown.

### 3.3. Proposed Sintering Mechanism

#### 3.3.1. Melting Temperature

As discussed in Section 3.1, the ZnAl<sub>2</sub>O<sub>4</sub> sample containing the Cu<sub>3</sub>Nb<sub>2</sub>O<sub>8</sub> additive began to densify at a low temperature (885 °C, Figure 2). LTCC materials normally

contain large quantities of glass, and densification is assumed to occur through liquid-phase sintering. Therefore, densification normally commences at a temperature above the melting point (eutectic temperature); hence, the melting temperatures of  $\text{Cu}_3\text{Nb}_2\text{O}_8$ -additive/ $\text{ZnAl}_2\text{O}_4$  mixtures need to be considered in addition to that of the  $\text{Cu}_3\text{Nb}_2\text{O}_8$  additive. Figure 9a presents DTA curves of 100:0, 95:5, 90:10, 80:20, and 50:50 (*w/w*)  $\text{Cu}_3\text{Nb}_2\text{O}_8$ -additive/ $\text{ZnAl}_2\text{O}_4$  mixtures when heated at  $10^\circ\text{C}/\text{min}$ . The  $\text{Cu}_3\text{Nb}_2\text{O}_8$  additive melts at  $967^\circ\text{C}$ , which did not change dramatically for most  $\text{Cu}_3\text{Nb}_2\text{O}_8$ -additive/ $\text{ZnAl}_2\text{O}_4$  powder mixtures. Moreover, this temperature is much higher than that at which densification begins ( $\sim 885^\circ\text{C}$ , Figure 2), which suggests that densification occurs in the solid phase prior to liquid phase formation; this process was referred to as “solid-state-activated sintering” by German et al. [27,28]. The minimum melting temperature determined from the DTA curve of each sample was taken to be the liquid-phase formation temperature,  $T_m$  (K). Figure 9b depicts the relationship between  $T/T_m$  (where  $T$  (K) is the firing temperature) and the relative density of  $\text{ZnAl}_2\text{O}_4$  containing 4 wt.% of  $\text{Cu}_3\text{Nb}_2\text{O}_8$  held for 2, 24, and 384 h. A  $T/T_m$  ratio above 1.00 indicates the formation of a liquid phase, while a value below 1.00 reveals that densification occurs solely through a solid-state mechanism. Samples at all retention times had relative densities of 98% or higher when  $T/T_m = 0.99$  ( $T = 1233$  K). Even with a  $T/T_m$  of 0.94 ( $T = 1183$  K), the sample held for 384 h achieved a relative density of 98% or higher. Hence,  $\text{ZnAl}_2\text{O}_4$  clearly underwent solid-state densification before liquification of the sintering aid; this system, therefore, underwent solid-state-activated sintering.

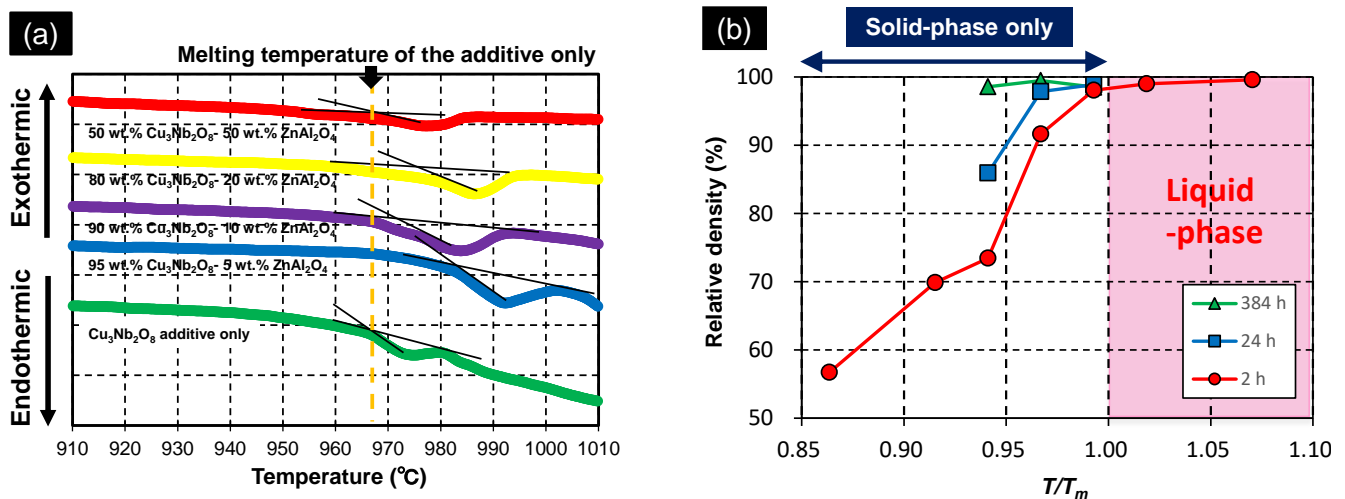


**Figure 9.** (a) Differential thermal analysis curves for  $\text{Cu}_3\text{Nb}_2\text{O}_8/\text{ZnAl}_2\text{O}_4$  mixtures acquired at  $10^\circ\text{C}/\text{min}$ . (b) Relative densities of  $\text{ZnAl}_2\text{O}_4$  containing 4 wt.% of  $\text{Cu}_3\text{Nb}_2\text{O}_8$  and held for 2, 24, and 384 h as a function of the firing-temperature/liquid-phase-formation temperature ratio ( $T/T_m$ ).

### 3.3.2. Degree of Solid Solution

German et al. [27,28] proposed “an ideal binary phase diagram for promoting liquid-phase sintering (LPS)” (Figure 10). The composition and firing temperature of the actual liquid-phase sintered body correspond to the blue dot in Figure 10. An ideal combination of composition and temperature results in high solid solubility in the liquid (eutectic liquid in this diagram) and low solubility of the liquid in the solid. A significantly lower melting temperature compared to that of the single component affords a processing temperature advantage. Therefore, we conclude that the conditions for promoting liquid-phase sintering is satisfied in our case, with  $\text{ZnAl}_2\text{O}_4$ , as the base material, exhibiting higher solid solubility in the  $\text{Cu}_3\text{Nb}_2\text{O}_8$  additive than that of the  $\text{Cu}_3\text{Nb}_2\text{O}_8$  additive in  $\text{ZnAl}_2\text{O}_4$ .

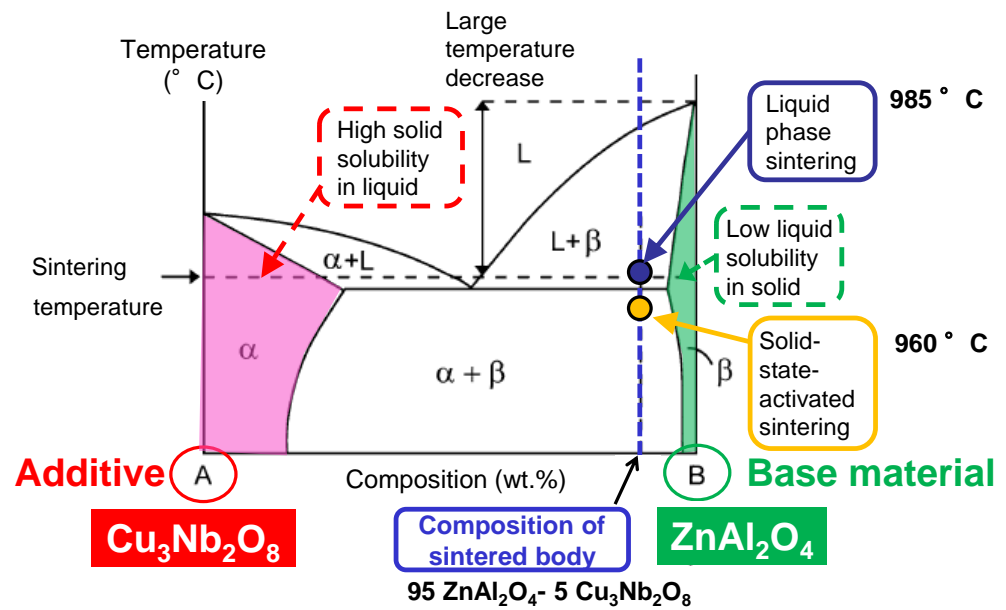


**Figure 10.** Ideal binary phase diagram for the liquid phase sintering of additive “A” and base material “B”.

Although the proposed theory (above) is only intended to describe the behavior of samples when liquid phases form, we believe that the described behavior also occurred in the solid state in this study (solid-state-activated sintering; yellow dot in Figure 10). However, as the phase diagram for this system has not yet been reported, we assumed a pseudo-binary phase diagram for the  $\text{ZnAl}_2\text{O}_4$ – $\text{Cu}_3\text{Nb}_2\text{O}_8$  system. Accordingly, we determined the degrees of solid dissolution of the  $\text{Cu}_3\text{Nb}_2\text{O}_8$  additive in  $\text{ZnAl}_2\text{O}_4$ , and  $\text{ZnAl}_2\text{O}_4$  in the  $\text{Cu}_3\text{Nb}_2\text{O}_8$  additive by monitoring lattice constant changes. Specifically, two types of mixed powder sample were heat-treated: 95 wt.%  $\text{Cu}_3\text{Nb}_2\text{O}_8$  additive + 5 wt.%  $\text{ZnAl}_2\text{O}_4$  (95C05Z), and 95 wt.%  $\text{Cu}_3\text{Nb}_2\text{O}_8$  additive + 5 wt.%  $\text{ZnAl}_2\text{O}_4$  (95Z05C). Changes in the XRD-measured lattice constants (unit cell volumes in this case) were determined as a function of heat-treatment temperature. The lattice constant of  $\text{Cu}_3\text{Nb}_2\text{O}_8$  after calcination at 835 °C for 2 h was measured for the 95C05Z sample, while the lattice constant of  $\text{ZnAl}_2\text{O}_4$  after calcination at 1100 °C for 4 h was measured for the 95Z05C sample, with values prior to heat treatment used as reference values for calculating change ratios.

Figure 11 displays the relationship between heat-treatment temperature and unit cell volume change ratios; the error bars show standard deviations ( $\sigma$ ). Figure 11a reveals that the  $\text{Cu}_3\text{Nb}_2\text{O}_8$  unit cell volume change ratio was approximately 0.25–0.55% higher than the reference value (at room temperature, 20 °C) when heat-treated at 585 °C or higher, although these results had relatively large error bars. This suggests that  $\text{Zn}^{2+}$ , which has a larger ionic radius (0.074 nm) than  $\text{Cu}^{2+}$  (0.073 nm) and  $\text{Nb}^{5+}$  (0.064 nm) when six-coordinated [29], was incorporated into  $\text{Cu}_3\text{Nb}_2\text{O}_8$ . It is not clear whether or not  $\text{Al}^{3+}$ , which has a smaller ionic radius (0.0535 nm when six-coordinated) than  $\text{Cu}^{2+}$  or  $\text{Nb}^{5+}$ , was incorporated in  $\text{Cu}_3\text{Nb}_2\text{O}_8$ . However,  $\text{Al}^{3+}$  was possibly an interstitial solid solution; in this case, a lower unit cell volume would not be expected for  $\text{Cu}_3\text{Nb}_2\text{O}_8$ .

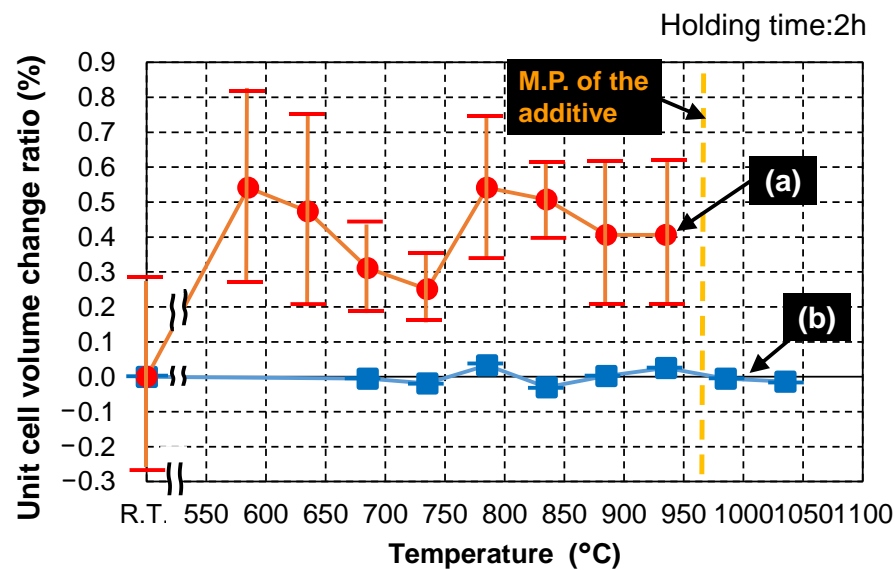


**Figure 11.** Unit cell volume change ratios of (a)  $\text{Cu}_3\text{Nb}_2\text{O}_8$  in a  $\text{Cu}_3\text{Nb}_2\text{O}_8$  sample containing 5 wt.% of  $\text{ZnAl}_2\text{O}_4$  (95C05Z), and (b)  $\text{ZnAl}_2\text{O}_4$  in a  $\text{ZnAl}_2\text{O}_4$  sample containing 5 wt.% of the  $\text{Cu}_3\text{Nb}_2\text{O}_8$  additive (95Z05C) as a function of heat-treatment temperature determined by XRD. Each particular temperature was held for 2 h.

On the other hand, Figure 11b shows almost no change in  $\text{ZnAl}_2\text{O}_4$  unit cell volume ratio (less than 0.05%) when heat-treated at 685–1035 °C, which suggests that  $\text{Cu}^{2+}$ , with a smaller ionic radius than  $\text{Zn}^{2+}$ , but larger than  $\text{Al}^{3+}$  [29], was not significantly incorporated into the Zn and Al sites of  $\text{ZnAl}_2\text{O}_4$ . Alternatively, it is possible that  $\text{Cu}^{2+}$  was simultaneously incorporated into both the Zn sites of  $\text{ZnAl}_2\text{O}_4$  and the Al sites of  $\text{ZnAl}_2\text{O}_4$ , which would offset any increase/decrease in the  $\text{ZnAl}_2\text{O}_4$  unit cell volume. Shigeno et al. [9] reported a unit cell volume change ratio of only ~0.1% for  $\text{Al}_2\text{O}_3$  when  $\text{Cu}^{2+}$  and  $\text{Ti}^{4+}$  were incorporated into  $\text{Al}_2\text{O}_3$  in an alumina sample containing 5 wt.% of the Cu–Ti–Nb–O sintering aid. In addition, Phillips et al. [30] reported that the unit cell volume of Ti-doped sapphire was also only ~0.1% larger than that of pure sapphire after annealing at 1600 °C for 24 h, which is similar to the results obtained in this study. Therefore, even if  $\text{Cu}^{2+}$  was incorporated into the Al sites of  $\text{ZnAl}_2\text{O}_4$ , we estimate that the unit cell volume change ratio (increase ratio) was only about 0.1%, while the change ratio (decrease ratio) in the unit cell volume associated with incorporating  $\text{Cu}^{2+}$  into the Zn sites was estimated to be ~0.1%. In other words, the  $\text{ZnAl}_2\text{O}_4$  unit cell volume change ratio (Figure 11b) was estimated to be smaller than that of  $\text{Cu}_3\text{Nb}_2\text{O}_8$  (Figure 11a) (0.25–0.55%).

To gain further insight into the Cu and Nb distributions, the  $\text{ZnAl}_2\text{O}_4$  particles were subjected to TEM–EDS before and after densification. Figure 12 shows TEM images and continuous EDS data for the intragranular additive elements (Cu and Nb) in sintered  $\text{ZnAl}_2\text{O}_4$  containing 5 wt.% of  $\text{Cu}_3\text{Nb}_2\text{O}_8$  fired at different temperatures (785 °C for 2 h, and 960 °C for 2 h). Each sample was subjected to six 30 min continuous EDS analyses at different intragranular locations; the values shown in parentheses denote standard deviations. Approximately  $0.12 \pm 0.04$  at.% Cu was detected in the  $\text{ZnAl}_2\text{O}_4$  sample (G06) fired at 785 °C for 2 h (Figure 12a). However, as shown in Figure 2a, this sample was not densified and is, therefore, considered to be a solid solution of Cu with the same valence as Zn (i.e., divalent). On the other hand, approximately  $0.37 \pm 0.23$  at.% Cu was detected in the densified  $\text{ZnAl}_2\text{O}_4$  sample (G07) fired at 960 °C for 2 h (Figure 12b). As evidenced by the standard deviations in Figure 12b and the EDS elemental map shown in Figure 4, Cu was not uniform and was sparsely distributed within the  $\text{ZnAl}_2\text{O}_4$  grain. The reason for this sparse distribution remains unknown; however, we presume that one of the reasons is that the Cu diffuses slowly during solid-state sintering, unlike in liquid-phase sintering. Nonetheless, we can confirm that more Cu diffused into the densified

ZnAl<sub>2</sub>O<sub>4</sub> grains than in grains before densification, suggesting that Cu was incorporated into ZnAl<sub>2</sub>O<sub>4</sub> not only at Zn sites but also at some Al sites. In contrast, the amounts of Nb were determined to be much less than 0.1 at.%, which is regarded to be the detection limit of the EDS instrument used. No clear difference in this value was observed before and after densification; therefore, while we cannot provide a definitive conclusion because only local analyses were performed, we presume that Nb atoms were not present within the ZnAl<sub>2</sub>O<sub>4</sub> particle grains.

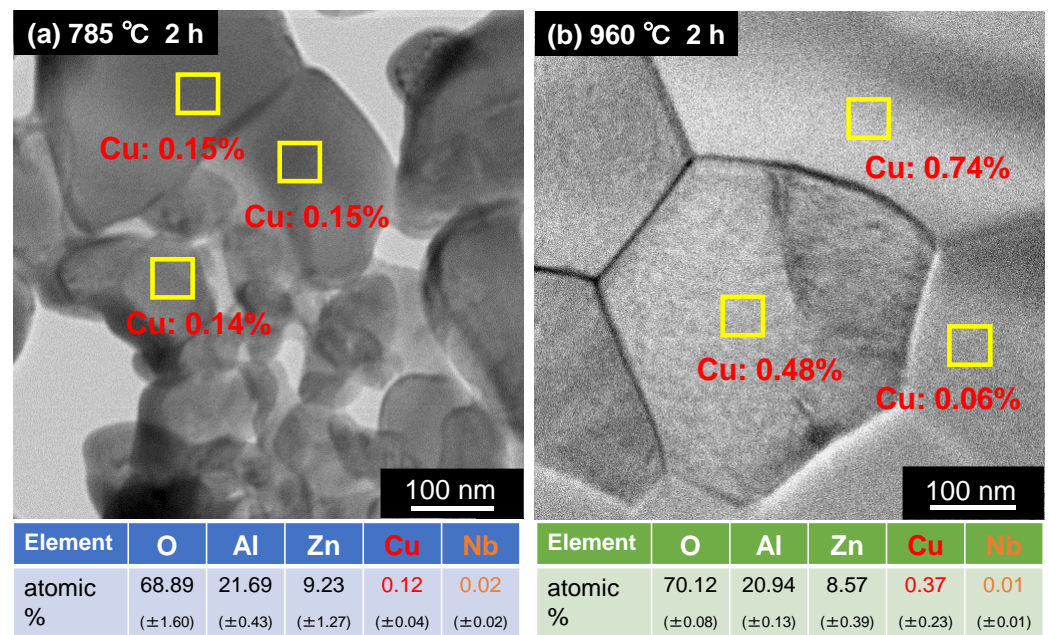
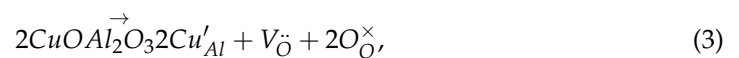
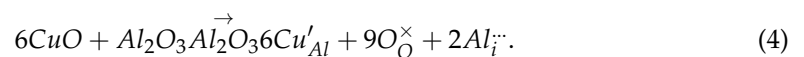


**Figure 12.** TEM images and EDS data (including standard deviation:  $\sigma$ ) for intragranular atoms (O, Al, Zn, Cu, and Nb) in sintered ZnAl<sub>2</sub>O<sub>4</sub> containing 5 wt.% of Cu<sub>3</sub>Nb<sub>2</sub>O<sub>8</sub> fired at (a) 785 °C for 2 h (G06), and (b) 960 °C for 2 h (G07).

The abovementioned results reveal that ZnAl<sub>2</sub>O<sub>4</sub> mainly densified with the help of defects formed by the substitution of Cu<sup>2+</sup> for Al<sup>3+</sup> in the ZnAl<sub>2</sub>O<sub>4</sub> lattice in the solid state at 835–960 °C, and they are believed to have been generated by the following reactions (Kröger–Vink notation):



and



Reaction (3) assumes defects due to vacancy formation, while Reaction (4) assumes defects due to interstitial ion formation. In the present study, oxygen vacancies ( $V_{\text{O}}^{\bullet\bullet}$  in Reaction (3)) or interstitial Al<sup>3+</sup> ( $\text{Al}_i^{\bullet\bullet}$  in Reaction (4)) were the main defects, as indicated by the significantly higher Cu concentration in the densified ZnAl<sub>2</sub>O<sub>4</sub> grains. Nb atoms are assumed to assist in increasing the diffusion rate of Cu<sup>2+</sup> by lowering the melting temperature of the sintering additive. The addition of Nb<sub>2</sub>O<sub>5</sub> to CuO lowered the melting temperature from 1025 to 967 °C. Furthermore, although the ionic radius of Nb<sup>5+</sup> is relatively close to that of Al<sup>3+</sup>, they cannot substitute into Al<sup>3+</sup> sites due to the +2 difference in valence.

The abovementioned results suggest that our system is qualitatively consistent with the “ideal binary phase diagram of LPS” advocated by German et al. [27,28]; therefore, they support the solid-state-activated sintering mechanism.

### 3.3.3. Solid-State-Activated Sintering Model in This Study

A schematic of the solid-state-activated sintering mechanism in this study is shown in Figure 13. Fine  $\text{ZnAl}_2\text{O}_4$  particles are gradually incorporated into the additive at temperatures below  $585^\circ\text{C}$ , without considerable densification (Figure 13a), and a solid solution forms at temperatures up to  $835^\circ\text{C}$ , at which point saturation occurs and  $\text{ZnAl}_2\text{O}_4$  reprecipitates. According to the Kelvin equation [31], reprecipitation occurs preferentially on the coarse particles, which are less soluble than the fine particles (Figure 13b) through a process known as “Ostwald ripening.” Necks form between coarse particles as they grow. The neck region is less soluble than the coarse particles; hence, reprecipitation occurs preferentially at the necks. TEM–EDS (Figure 12) revealed that the deposited  $\text{ZnAl}_2\text{O}_4$  was not pure, and those small quantities of additive components ( $\text{Cu}^{2+}$ ) were incorporated into the  $\text{Zn}^{2+}$  sites, as well as the  $\text{Al}^{3+}$  sites of the  $\text{ZnAl}_2\text{O}_4$  in neck regions. We presume that the incorporated atoms created defects (Al- or O-related defects) in the  $\text{ZnAl}_2\text{O}_4$  lattice that promote solid-phase diffusion between  $\text{ZnAl}_2\text{O}_4$  particles, thereby promoting sintering (Figure 13c). The solid solution particles of the additive probably formed an intergranular amorphous phase during densification [32], which reduced the grain-boundary energy of  $\text{ZnAl}_2\text{O}_4$ . As sintering occurs through solid-phase diffusion, long retention times are required; however, densification is guaranteed. Lastly, according to the TEM–EDS results (Figure 4), we conclude that most additive components segregated and remained in the intergranular amorphous phase and other crystal compounds at grain boundaries. Because the  $\text{ZnAl}_2\text{O}_4$  grains were larger after sintering for 384 h than after sintering for 2 h (Figure 8b,d,f), we conclude that the grains increased in size during sintering.

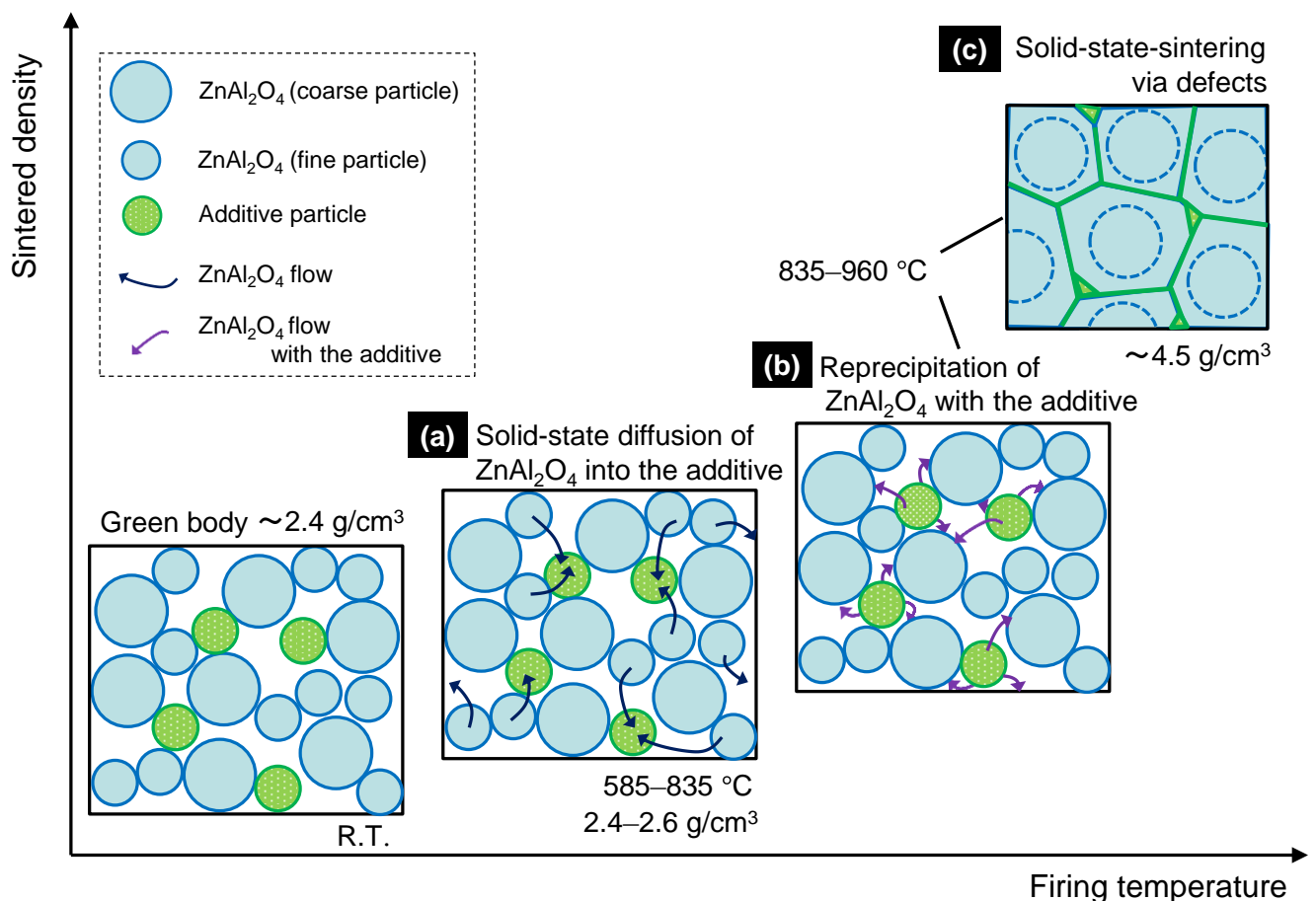


**Figure 13.** Solid-state-activated sintering model for  $\text{ZnAl}_2\text{O}_4$  containing 5 wt.% of  $\text{Cu}_3\text{Nb}_2\text{O}_8$ . (a) Solid-state diffusion of  $\text{ZnAl}_2\text{O}_4$  into the additive, (b) Recipitation of  $\text{ZnAl}_2\text{O}_4$  with the additive, and (c) Solid-state-sintering via defects.

#### 4. Conclusions

The addition of a small amount of the calcined  $\text{Cu}_3\text{Nb}_2\text{O}_8$  sintering aid to  $\text{ZnAl}_2\text{O}_4$ , a highly thermally conductive dielectric material, successfully enabled  $\text{ZnAl}_2\text{O}_4$  sintering at (low) temperatures below the melting point of silver (961 °C), resulting in better dielectric properties (in particular, a quality factor by resonant frequency product  $Q \times f$ ) than those obtained by the addition of the non-calcined  $\text{CuO-Nb}_2\text{O}_5$  (in a 3:2 Cu:Nb molar ratio) sintering aid. In addition, the sample fired at 960 °C exhibited more suitable dielectric characteristics, such as a relative permittivity  $\epsilon_r$  of 9.2, a  $Q \times f$  of 105,000 GHz, and a temperature coefficient of resonant frequency  $\tau_f$  of  $-56 \text{ ppm} \cdot \text{K}^{-1}$  when the holding time was prolonged from 2 h to 384 h. The sample exhibited a thermal conductivity of  $10.1 \text{ W} \cdot \text{m}^{-1} \cdot \text{K}^{-1}$ , which exceeds that of conventional LTCCs ( $\sim 2\text{--}7 \text{ W} \cdot \text{m}^{-1} \cdot \text{K}^{-1}$ ). Moreover, we suggest that this system underwent solid-state-activated sintering by specifically incorporating  $\text{Cu}^{2+}$  in the  $\text{ZnAl}_2\text{O}_4$  lattice, in which densification was virtually complete even when the sintering aid remained in the solid state. The Nb component presumably indirectly affected the  $\text{Cu}^{2+}$  diffusion rate by lowering the melting temperature of the additive.

Future studies will further elucidate the mechanism associated with solid-state-activated sintering in this system and apply the acquired knowledge to the fabrication of various Al-based ceramic materials.

**Author Contributions:** K.S. conceptualized and designed the experiments; K.S. and T.Y. performed the experiments; K.S., T.Y. and H.F. analyzed the data. K.S. wrote the manuscript. All authors have read and agreed to the published version of the manuscript.

**Funding:** This research was funded by the Electric Technology Research Foundation of Chugoku.

**Institutional Review Board Statement:** Not applicable.

**Informed Consent Statement:** Not applicable.

**Data Availability Statement:** Data will be made available upon reasonable request.

**Acknowledgments:** We are indebted to Hirotaka Ogawa and Akinori Kan of Meijo University for their assistance with the dielectric property experiments. We also deeply thank Keisuke Ura of the Industrial Technology Institute, Miyagi Prefectural Government, for his assistance with calculating the unit cell volumes of  $\text{Cu}_3\text{Nb}_2\text{O}_8$  from the XRD data.

**Conflicts of Interest:** The authors declare no conflict of interest.

#### References

1. Imanaka, Y. *Multilayered Low Temperature Cofired Ceramics (LTCC) Technology*; Springer: New York, NY, USA, 2005; pp. 1–18.
2. Sebastian, M.T. *Dielectric Materials for Wireless Communication*; Elsevier: New York, NY, USA, 2008; pp. 445–512.
3. Sebastian, M.T.; Wang, H.; Jantunen, H. Low temperature co-fired ceramics with ultra-low sintering temperature: A review. *Curr. Opin. Solid State Mater. Sci.* **2016**, *20*, 151–170. [[CrossRef](#)]
4. Sebastian, M.T.; Jantunen, H. Low loss dielectric materials for LTCC applications. *Int. Mater. Rev.* **2008**, *53*, 58–90. [[CrossRef](#)]
5. Induja, I.J.; Abhilash, P.; Arun, S.; Surendran, K.P.; Sebastian, M.T. LTCC tapes based on  $\text{Al}_2\text{O}_3$ -BBSZ glass with improved thermal conductivity. *Ceram. Int.* **2015**, *41*, 13572–13581. [[CrossRef](#)]
6. Yin, L.; Yang, L.; Yang, W.; Guo, Y.; Ma, K.; Li, S.; Zhang, J. Thermal design and analysis of multi-chip LED module with ceramic substrate. *Solid-State Electron.* **2010**, *54*, 1520–1524. [[CrossRef](#)]
7. Shimizu, M.; Tomioka, S.; Yoshida, N.; Kameyama, I.; Okuda, K. Varistor and Its Manufacturing Method. Japanese Patent Publication No. 2015-156406, 2015.
8. Shigeno, K.; Katsumura, H.; Kagata, H.; Asano, H.; Inoue, O. Preparation and characterization of low temperature sintered alumina by  $\text{CuO-TiO}_2\text{-Nb}_2\text{O}_5\text{-Ag}_2\text{O}$  additives. *Ferroelectrics* **2007**, *356*, 189–196. [[CrossRef](#)]
9. Shigeno, K.; Kuraoka, Y.; Asakawa, T.; Fujimori, H. Sintering mechanism of low-temperature co-fired alumina featuring superior thermal conductivity. *J. Am. Ceram. Soc.* **2021**, *104*, 2017–2029. [[CrossRef](#)]
10. Surendran, K.P.; Santha, N.; Mohanan, P.; Sebastian, M.T. Temperature stable low loss ceramic dielectrics in  $(1-x)\text{ZnAl}_2\text{O}_4\text{-xTiO}_2$  system for microwave substrate applications. *Eur. Phys. J.* **2004**, *B41*, 301–306. [[CrossRef](#)]
11. Surendran, K.P.; Sebastian, M.T.; Manjusha, M.V.; Philip, J. A low loss, dielectric substrate in  $\text{ZnAl}_2\text{O}_4\text{-TiO}_2$  system for microelectronic applications. *J. Appl. Phys.* **2005**, *98*, 044101. [[CrossRef](#)]
12. Roshni, S.; Sebastian, M.T.; Surendran, K.P. Can zinc aluminate-titania composite be an alternative for alumina as microelectronic substrate? *Sci. Rep.* **2017**, *7*, 40839. [[CrossRef](#)]

13. Fu, P.; Wang, Z.Y.; Lin, Z.D.; Liu, Y.Q.; Roy, V.A.L. The microwave dielectric properties of transparent  $\text{ZnAl}_2\text{O}_4$  ceramics fabricated by spark plasma sintering. *J. Mater. Sci. Mater. Electron.* **2017**, *28*, 9589–9595. [[CrossRef](#)]
14. Thomas, S.; Sebastian, M.T. Effect of  $\text{B}_2\text{O}_3$ - $\text{Bi}_2\text{O}_3$ - $\text{SiO}_2$ - $\text{ZnO}$  glass on the sintering and microwave dielectric properties of  $0.83\text{ZnAl}_2\text{O}_4$ - $0.17\text{TiO}_2$ . *Mater. Res. Bull.* **2008**, *43*, 843–851. [[CrossRef](#)]
15. Takahashi, S.; Kan, A.; Ogawa, H. Microwave dielectric properties and cation distributions of  $\text{Zn}_{1-3x}\text{Al}_{2+2x}\text{O}_4$  ceramics with defect structures. *J. Eur. Ceram. Soc.* **2017**, *37*, 3059–3064. [[CrossRef](#)]
16. Lan, X.-K.; Li, J.; Zou, Z.-Y.; Xie, M.-Q.; Fan, G.-F.; Lu, W.-Z.; Lei, W. Improved sinterability and microwave dielectric properties of  $[\text{Zn}_{0.5}\text{Ti}_{0.5}]^{3+}$ -doped  $\text{ZnAl}_2\text{O}_4$  spinel solid solution. *J. Am. Ceram. Soc.* **2019**, *102*, 5952–5957. [[CrossRef](#)]
17. Shigeno, K.; Kaneko, S.; Nakashima, H.; Suenaga, K.; Fujimori, H. Low-temperature sintering of gahnite ceramic using Cu-Nb-O additive and evaluation of dielectric and thermal properties. *J. Electron. Mater.* **2020**, *49*, 6046–6054. [[CrossRef](#)]
18. Nunes, S.I.; Bradt, R.C. Grain growth of ZnO in  $\text{ZnO-Bi}_2\text{O}_3$  ceramics with  $\text{Al}_2\text{O}_3$  additions. *J. Am. Ceram. Soc.* **1995**, *78*, 2469–2475. [[CrossRef](#)]
19. Kim, D.-W.; Kim, I.-T.; Park, B.; Hong, K.-S.; Kim, J.-H. Microwave dielectric properties of  $(1-x)\text{Cu}_3\text{Nb}_2\text{O}_8-x\text{Zn}_3\text{Nb}_2\text{O}_8$  ceramics. *J. Mater. Res.* **2001**, *16*, 1465–1470. [[CrossRef](#)]
20. Matsui, K.; Matsumoto, A.; Uehara, M.; Enomoto, N.; Hojo, J. Sintering kinetics at isothermal shrinkage: Effect of specific surface area on the initial sintering stage of fine zirconia powder. *J. Am. Ceram. Soc.* **2007**, *90*, 44–49. [[CrossRef](#)]
21. Takada, T.; Wang, S.F.; Yoshikawa, S.; Jang, S.-J.; Newnham, R.E. Effect of glass addition on  $\text{BaO-TiO}_2\text{-WO}_3$  microwave ceramics. *J. Am. Ceram. Soc.* **1994**, *77*, 1909–1916. [[CrossRef](#)]
22. Hakki, B.W.; Coleman, P.D. A dielectric resonator method of measuring inductive capacities in the millimeter range. *IRE Trans. Microw. Theory Tech.* **1960**, *8*, 402–410. [[CrossRef](#)]
23. Yamaguchi, T. Characterization techniques of ceramic: Properties of sintered bodies. *Ceram. Jpn.* **1984**, *19*, 520–529.
24. Tamura, H. Microwave dielectric losses caused by lattice defects. *J. Eur. Ceram. Soc.* **2006**, *26*, 1775–1780. [[CrossRef](#)]
25. Zheng, C.W.; Fan, X.C.; Chen, X.M. Analysis of infrared reflection spectra of  $(\text{Mg}_{1-x}\text{Zn}_x)\text{Al}_2\text{O}_4$  microwave dielectric ceramics. *J. Am. Ceram. Soc.* **2008**, *91*, 490–493. [[CrossRef](#)]
26. Penn, S.J.; Alford, N.M.; Templeton, A.; Wang, X.; Xu, M.; Reece, M.; Schrapel, K. Effect of porosity and grain size on the microwave dielectric properties of sintered alumina. *J. Am. Ceram. Soc.* **1997**, *80*, 1885–1888. [[CrossRef](#)]
27. German, R.M.; Farooq, S.; Kippit, C.M. Kinetics of liquid sintering. *Mater. Sci. Eng. A* **1988**, *105/106*, 215–224. [[CrossRef](#)]
28. German, R.M.; Suri, P.; Park, S.J. Liquid phase sintering. *J. Mater. Sci.* **2009**, *44*, 1–39. [[CrossRef](#)]
29. Shannon, R.D. Revised effective ionic radii and systematic studies of interatomic distances in halides and chalcogenides. *Acta Crystallogr. A* **1976**, *32*, 751–767. [[CrossRef](#)]
30. Phillips, D.S.; Mitchell, T.E.; Heuer, A.H. Precipitation in star sapphire III. Chemical effects accompanying precipitation. *Philos. Mag.* **1980**, *A42*, 417–432. [[CrossRef](#)]
31. Kingery, W.D.; Bowen, H.K.; Uhlmann, D.R. *Introduction to Ceramics*, 2nd ed.; Wiley: New York, NY, USA, 1976; pp. 413–429.
32. Liu, H.-H.; Jean, J.-H. Processing and properties of a low-fire, high-thermal-conductivity alumina with  $\text{CuTiNb}_2\text{O}_8$ . *Int. J. Ceram. Eng. Sci.* **2020**, *2*, 38–45. [[CrossRef](#)]